ARTICLE

doi:10.1038/nature25451

α-Klotho is a non-enzymatic molecular scaffold for FGF23 hormone signalling

Gaozhi Chen[1,2*], Yang Liu[2*], Regina Goetz[2], Lili Fu[1,2], Seetharaman Jayaraman[3], Ming-Chang Hu[4], Orson W. Moe[4], Guang Liang[1], Xiaokun Li[1] & Moosa Mohammadi[2]

The ageing suppressor α-klotho binds to the fibroblast growth factor receptor (FGFR). This commits FGFR to respond to FGF23, a key hormone in the regulation of mineral ion and vitamin D homeostasis. The role and mechanism of this co-receptor are unknown. Here we present the atomic structure of a 1:1:1 ternary complex that consists of the shed extracellular domain of α-klotho, the FGFR1c ligand-binding domain, and FGF23. In this complex, α-klotho simultaneously tethers FGFR1c by its D3 domain and FGF23 by its C-terminal tail, thus implementing FGF23–FGFR1c proximity and conferring stability. Dimerization of the stabilized ternary complexes and receptor activation remain dependent on the binding of heparan sulfate, a mandatory cofactor of paracrine FGF signalling. The structure of α-klotho is incompatible with its purported glycosidase activity. Thus, shed α-klotho functions as an on-demand non-enzymatic scaffold protein that promotes FGF23 signalling.

Endocrine FGF23 regulates phosphate and vitamin D homeostasis by reducing the cell surface expression of sodium phosphate co-transporters and by repressing transcription of rate-limiting enzymes for vitamin D biosynthesis[1,2] in the kidney. FGF23 exerts its metabolic functions by binding and activating FGFR tyrosine kinases[3] in an α-klotho co-receptor dependent fashion. The extracellular domain of a prototypical FGFR consists of three immunoglobulin-like domains: D1, D2 and D3. The membrane proximal portion comprising D2, D3 and the D2–D3 linker (FGFR^{ecto}) is both necessary and sufficient for FGF ligand binding[4,5]. Tissue-specific alternative splicing in the D3 domain of FGFR1–FGFR3 generates 'b' and 'c' isoforms, each with distinct ligand-binding specificity[5,6]. α-klotho, fortuitously discovered as an ageing-suppressor gene[7], is a single-pass transmembrane protein with an extracellular domain composed of two tandem domains (KL1 and KL2), each with notable homology to family 1 glycosidases[8] (Extended Data Fig. 1a). Membrane-bound α-klotho (α-klotho^{TM}) associates with cognate FGFRs of FGF23, namely the 'c' splice isoforms of FGFR1 and FGFR3 (FGFR1c and FGFR3c) and FGFR4[9–12]. This enables them to bind and respond to FGF23[9,11,12]. α-klotho^{TM} is predominantly expressed in the kidney distal tubules, the parathyroid gland, and the brain choroid plexus[7,13], and this is considered to determine the target tissue specificity of FGF23[11,12]. Cleavage of α-klotho^{TM} by ADAM proteases[14,15] in kidney distal tubules sheds the α-klotho ectodomain (α-klotho^{ecto}; Extended Data Fig. 1a) into body fluids, for example, serum, urine and cerebrospinal fluid[16–19]. α-Klotho^{ecto} is thought to lack co-receptor activity and act as a circulating anti-ageing hormone independently of FGF23[20,21]. A plethora of activities has been attributed to shed α-klotho^{ecto}, the bulk of which require a purported intrinsic glycosidase activity[22–25].

Here we show that circulating α-klotho^{ecto} is an on-demand bona fide co-receptor for FGF23, and determine its crystal structure in complex with FGFR1c^{ecto} and FGF23. The structure reveals that α-klotho serves as a non-enzymatic scaffold that simultaneously tethers FGFR1c and FGF23 to implement FGF23–FGFR1c proximity and hence stability. Surprisingly, heparan sulfate (HS), a mandatory cofactor for paracrine FGFs, is still required as an ancillary cofactor to promote the formation of a symmetric 2:2:2:2 FGF23–FGFR1c–Klotho-HS quaternary signalling complex.

Soluble α-klotho^{ecto} acts as a co-receptor for FGF23

To determine whether soluble α-klotho^{ecto} can support FGF23 signalling, α-klotho-deficient HEK293 cells, which naturally express FGFRs, were incubated with a concentration of α-klotho^{ecto} sufficient to drive all available cell-surface cognate FGFRs into binary complexed form. After brief rinses with PBS, the cells were stimulated with increasing concentrations of FGF23. In parallel, a HEK293 cell line that overexpresses membrane-bound α-klotho (HEK293-α-klotho^{TM}) was treated with increasing concentrations of FGF23. The dose–response for FGF23-induced ERK phosphorylation in α-klotho^{ecto}-pretreated untransfected HEK293 cells was similar to that observed in HEK293-α-klotho^{TM} cells (Extended Data Fig. 1b, top), suggesting that α-klotho^{ecto} can serve as a co-receptor for FGF23. Pre-treatment of HEK293-α-klotho^{TM} cells with α-klotho^{ecto} did not result in any further increase in FGF23 signalling, indicating that all cell-surface FGFRs in this cell line were in binary FGFR–α-klotho^{TM} form (Extended Data Fig. 1b, bottom). We conclude that soluble and transmembrane forms of α-klotho possess a similar capacity to support FGF23 signalling. Consistent with these results, injection of wild-type mice with α-klotho^{ecto} protein led to an increase in renal phosphate excretion and a decrease in serum phosphate (Extended Data Fig. 1c). Notably, it also led to a 1.5-fold increase in *Egr1* transcripts in the kidney (Extended Data Fig. 1d), demonstrating that α-klotho^{ecto} can serve as a bona fide co-receptor to support FGF23 signalling in renal proximal tubules. In light of these data, we propose that the pleiotropic anti-ageing effects of α-klotho are all dependent on FGF23.

[1]Chemical Biology Research Center, School of Pharmaceutical Sciences, Wenzhou Medical University, Wenzhou, Zhejiang 325035, China. [2]Department of Biochemistry & Molecular Pharmacology, New York University School of Medicine, New York, New York 10016, USA. [3]New York Structural Biology Center, New York, New York 10027, USA. [4]Departments of Internal Medicine and Physiology, and Charles and Jane Pak Center of Mineral Metabolism and Clinical Research, University of Texas Southwestern Medical Center, Dallas, Texas 75390, USA.
*These authors contributed equally to this work.

Structural basis of α-klotho co-receptor function

We solved the crystal structure of a human 1:1:1 FGF23–FGFR1c^{ecto}–α-klotho^{ecto} ternary complex at 3.0 Å resolution (Extended Data Table 1). In this complex, α-klotho^{ecto} serves as a massive scaffold, tethering both FGFR1c and FGF23 to itself. In doing so, α-klotho^{ecto} enforces FGF23–FGFR1c proximity and thus augments FGF23–FGFR1c binding affinity (Fig. 1). The overall geometry of the ternary complex is compatible with its formation on the cell surface (Extended Data Fig. 2a).

The binary FGF23–FGFR1c^{ecto} complex adopts a canonical FGF–FGFR complex topology, in which FGF23 is bound between the D2 and D3 domains of the receptor, engaging both these domains and a short interdomain linker (Extended Data Fig. 3a). However, compared to paracrine FGFs, FGF23 makes fewer or weaker contacts with the D3 domain and D2–D3 linker, explaining the inherently low affinity of FGF23 for FGFR1c (Extended Data Fig. 3b, c). Notably, analysis of the binding interface between FGF23 and FGFR1c D3 in the crystal structure reveals specific contacts between FGF23 and a serine residue uniquely present in the 'c' splice isoforms of FGFR1–FGFR3 and in FGFR4 (Extended Data Fig. 4a). Indeed, replacing this 'c'-isoform-specific serine residue with a 'b'-isoform-specific tyrosine impaired FGF23 signalling (Extended Data Fig. 4b, c). We conclude that the FGFR binding specificity inherent to FGF23 operates alongside that of α-klotho (Extended Data Fig. 4d, e) to restrict FGF23 signalling to the 'c' splice isoforms and FGFR4[11,12].

In the ternary complex, α-klotho^{ecto} exists in an extended conformation. Consistent with their sequence homology to the glycoside hydrolase A clan[8], the α-klotho KL1 (Glu34 to Phe506) and KL2 (Leu515 to Ser950) domains each assume a $(\beta\alpha)_8$ triosephosphate isomerase (TIM) barrel fold consisting of an inner eight-stranded parallel β-barrel and eight surrounding α-helices (Fig. 2a and Extended Data Fig. 5a). The two KL domains are connected by a short, proline-rich and hence stiff linker (Pro507 to Pro514) (Fig. 1a, b). KL1 sits atop KL2, engaging it via a few interdomain contacts involving the N terminus preceding the β1 strand and the α7 helix of KL1, and the β5α5 and β6α6 loops and α7 helix of KL2 (Extended Data Fig. 2b). Notably, one of the interdomain contacts is mediated by a Zn^{2+} ion (Fig. 3c and Extended Data Fig. 2b, c). These contacts stabilize the observed elongated conformation of α-klotho^{ecto}, creating a deep cleft between the two KL domains. This merges with a wide-open central β-barrel cavity in KL2, and forms a large binding pocket that tethers the distal C-terminal tail of FGF23 past the 176-Arg-His-Thr-Arg-179 proteolytic cleavage site (Fig. 1b). Meanwhile, the long β1α1 loop of KL2 (Fig. 2a) protrudes as much as 35 Å away from the KL2 core to latch onto the FGFR1c D3 domain, thus anchoring the receptor to α-klotho (Fig. 1b). Accordingly, we have named this KL2 loop the receptor binding arm (RBA; residues 530–578; Extended Data Fig. 5a).

We superimposed the TIM barrels of KL1 and KL2 onto that of klotho-related protein (KLrP, also known as GBA3), the cytosolic member of the klotho family with proven glycosylceramidase activity[26]. This comparison revealed major conformational differences in the loops surrounding the entrance to the catalytic pocket in KL1 and KL2 (Fig. 2b and Extended Data Fig. 5b–d). Moreover, both KL domains lack one of the key catalytic glutamates deep within the putative catalytic pocket. These substantial differences are incompatible with an intrinsic glycosidase activity for α-klotho[22–25]. Indeed, α-klotho^{ecto} failed to hydrolyse substrates for both sialidase and β-glucuronidase *in vitro* (Fig. 2c). Together, our data define α-klotho as the only known example of a TIM barrel protein that serves purely as a non-enzymatic molecular scaffold.

Binding interface between α-klotho and FGFR1c

The interface between α-klotho RBA and FGFR1c D3 (Fig. 3a) buries over 2,200 Å^2 of solvent-exposed surface area, which is consistent with the high affinity of α-klotho binding to FGFR1c (dissociation constant (K_d) = 72 nM)[10]. At the distal tip of the RBA, residues 547-Tyr-Leu-Trp-549 and 556-Ile-Leu-Arg-558 form a short β-strand pair

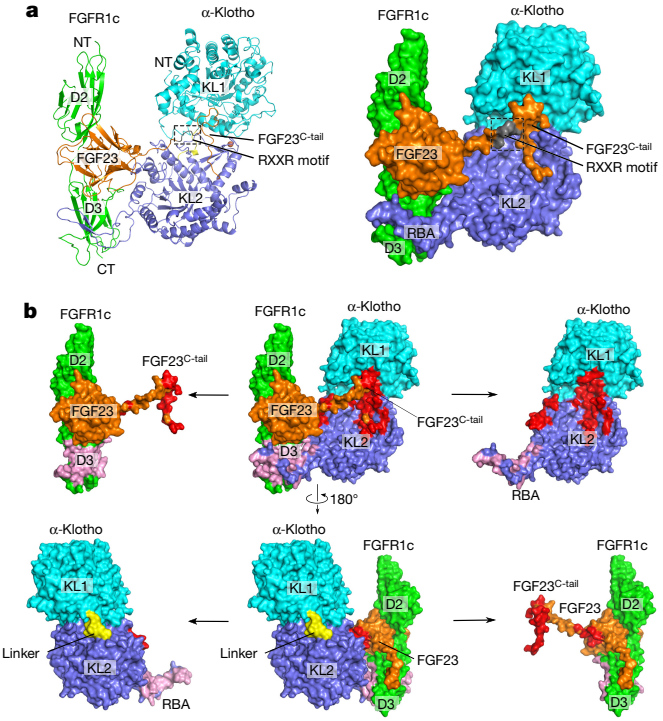

Figure 1 | Overall topology of the FGF23–FGFR1c^{ecto}–α-klotho^{ecto} complex. a, Cartoon (left) and surface representation (right) of the ternary complex structure. The α-klotho KL1 (cyan) and KL2 (blue) domains are joined by a short proline-rich linker (yellow; not visible in the surface presentation). FGF23 is in orange with its proteolytic cleavage motif in grey. FGFR1c is in green. CT, C terminus; NT, N terminus. **b**, Binding interfaces between α-klotho^{ecto} and the FGF23–FGFR1c^{ecto} complex. The ternary complex (centre) is shown in two different orientations related by a 180° rotation along the vertical axis. FGF23–α-klotho^{ecto} (red) and FGFR1c^{ecto}–α-klotho^{ecto} (pink) interfaces are visualized by pulling α-klotho^{ecto} and the FGF23–FGFR1c^{ecto} complex away from each other. The separated components are shown to the left and right of the ternary complex.

(RBA-β1:RBA-β2) as their hydrophobic side chains are immersed in a wide hydrophobic groove between the four-stranded βC′-βC-βF-βG sheet and the βC-βC′ loop of FGFR1c D3 (Fig. 3b, top). The RBA-β1:RBA-β2 strand pair forms an extended β-sheet with the βC′-βC-βF-βG sheet of D3 as the backbone atoms of RBA-β1 and D3 βC′ make three hydrogen bonds that further augment the interface (Fig. 3b, bottom). Residues at the proximal end of the RBA engage a second smaller binding pocket at the bottom edge of D3 next to the hydrophobic groove (Extended Data Fig. 6a, b). Both α-klotho binding pockets in the receptor D3 domain differ between 'b' and 'c' splice isoforms. Leu342, for example, is strictly conserved in the 'c' splice isoforms of FGFR1–FGFR3 and FGFR4. This explains the previously described binding selectivity of α-klotho for this subset of FGFRs[9,11,12] (Extended Data Fig. 4a).

Consistent with the crystal structure, soluble α-klotho lacking the RBA (α-klotho$^{ecto/\Delta RBA}$) failed to form a binary complex with FGFR1c^{ecto} in solution (Fig. 4a) and hence could not support FGF23 signalling (Fig. 4b). Likewise, membrane-bound α-klotho lacking the RBA (α-klotho$^{TM/\Delta RBA}$) was also disabled in acting as a FGF23 co-receptor (Fig. 4b). Importantly, α-klotho$^{ecto/\Delta RBA}$ did not exhibit any phosphaturic activity *in vivo* (Extended Data Fig. 7a). On the contrary, the α-klotho$^{ecto/\Delta RBA}$ mutant antagonized the activity of native α-klotho by sequestering FGF23 into functionally inactive binary complexes, that is, by acting as an FGF23 ligand trap (Extended Data Fig. 7). These data refute the concept that α-klotho^{ecto} functions as an FGF23-independent phosphaturic enzyme[24]. Our conclusion is supported by a gene knockout study that compared the phenotypes of mice with knockout of FGF23 (*Fgf23*$^{-/-}$), mice with knockout of α-klotho (*Kl*$^{-/-}$) and double-knockout mice (*Fgf23*$^{-/-}$*Kl*$^{-/-}$)[27].

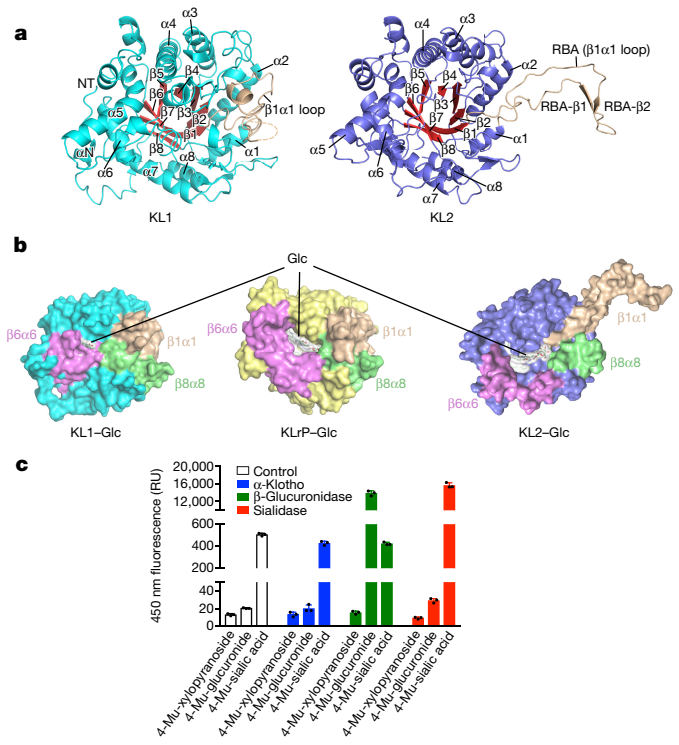

Figure 2 | α-Klotho is a non-enzymatic molecular scaffold. **a**, Triosephosphate isomerase (TIM) barrel topology of the α-klotho KL1 and KL2 domains. KL1 is in the same orientation as in Fig. 1a, whereas KL2 has been superimposed onto KL1 and has thus been reoriented. The eight alternating β-strands (red) and α-helices (cyan/blue) that define the TIM barrel are labelled according to the standard nomenclature for the TIM fold[8]. KL1 and KL2 differ markedly in the conformation of the β1α1 loop (wheat). In KL2, this loop protrudes away from the TIM barrel and serves as a receptor binding arm (RBA; Fig. 1). **b**, Molecular surfaces of KLrP–glucosylceramide (Glc) (centre; KLrP in yellow), KL1–Glc (left; KL1 in cyan) and KL2–Glc (right; KL2 in blue). Binding of Glc to KL1 and KL2 was simulated by superimposing KL1 and KL2 onto KLrP–Glc. In all cases, Glc is shown as pale grey sticks or surface. The divergent conformation of the β6α6 loop (pink) in KL1 almost seals off the entrance to the catalytic pocket, while the divergent conformations of the β1α1 (RBA; wheat), β6α6 (pink) and β8α8 (green) loops in KL2 leave the central barrel cavity in KL2 in a more solvent-exposed state that is less capable of ligating substrate (see also Extended Data Fig. 5). **c**, Glycosidase activity of α-klotho^{ecto}, sialidase and β-glucuronidase. Data are mean and s.d. Dots denote individual data points; $n = 3$ independent experiments. RU, relative units.

Binding interface between α-klotho and FGF23

Regions from both KL domains act together to recruit FGF23 (Fig. 1b), thus explaining why only an intact α-klotho ectodomain is capable of supporting FGF23 signalling[12,28]. The interactions between FGF23 and α-klotho result in the burial of a large amount of solvent-exposed surface area (2,732 Å^2), of which nearly two-thirds (1,961 Å^2) are buried between the FGF23 C-terminal tail and α-klotho, and the remaining one-third is buried between the FGF23 core and α-klotho (Fig. 3a). At the interface between α-klotho and the FGF23 C-terminal tail, FGF23 residues 188-Asp-Pro-Leu-Asn-Val-Leu-193 adopt an unusual cage-like conformation (Fig. 3a, c), which is tethered by residues from both KL domains via hydrogen bonds and hydrophobic contacts deep inside the KL1–KL2 cleft (Fig. 3c). Further downstream, the side chains of Lys194, Arg196 and Arg198 of the FGF23 C-terminal tail dip into the central barrel cavity of KL2, making hydrogen bonds with several α-klotho residues (Fig. 3c). At the interface between the FGF23 β-trefoil core and α-klotho, residues from the β5β6 turn and the αC helix of FGF23 make hydrogen bonds and hydrophobic contacts with residues in the short β7α7 and β8α8 loops at the upper rim of the KL2 cavity (Extended Data Fig. 6a, c).

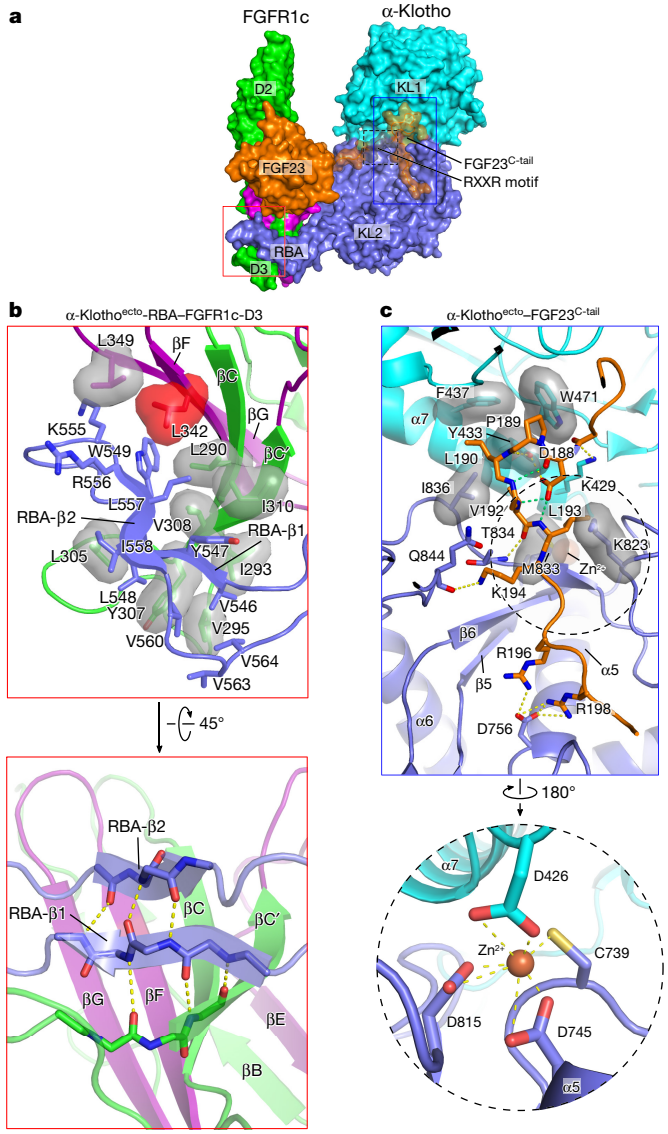

Figure 3 | α-Klotho simultaneously tethers FGFR1c by its D3 domain and FGF23 by its C-terminal tail. a, Ternary complex structure in surface representation. Colouring is as in Fig. 1a, except that the alternatively spliced region of FGFR1c is highlighted in purple. Red box denotes perimeter of interface between distal tip of α-klotho RBA and the hydrophobic FGFR1c D3 groove. Blue box denotes the perimeter of α-klotho–FGF23$^{C\text{-}tail}$ interface. **b**, RBA stretches out of the KL2 domain of α-klotho^{ecto} and latches onto the FGFR1c D3 domain. Top, interface between the distal tip of RBA and the D3 groove detailing hydrophobic interactions (grey transparent surfaces). Note that Leu342 (red) from the spliced region of the D3 groove is strictly conserved in 'c' splice isoforms of FGFR1–FGFR3 and FGFR4 and is mutated in Kallmann syndrome[36]. Bottom, close-up view of the extended β-sheet between the RBA-β1:RBA-β2 strand pair and the four-stranded β-sheet in D3 (βC′-βC-βF-βG). This structure forms via hydrogen bonding (dashed yellow lines) between backbone atoms of RBA-β1 and D3-βC′. **c**, Both KL domains of α-klotho^{ecto} participate in tethering of the flexible C-terminal tail of FGF23 (FGF23$^{C\text{-}tail}$). FGF23$^{C\text{-}tail}$ residues Asp188–Thr200 thread through the KL1–KL2 cleft and the β-barrel cavity of KL2. Of these residues, Asp188–Leu193 adopt a cage-like conformation that is partially stabilized by intramolecular hydrogen bonds (dashed green lines). Dashed yellow lines denote intermolecular hydrogen bonds; grey transparent surfaces denote hydrophobic interactions. Note that Tyr433 from the KL1 α7 helix deep inside the KL1–KL2 cleft has a prominent role in tethering the cage-like structure in the FGF23$^{C\text{-}tail}$ formed by Asp188–Leu193. Dashed circle (shown at greater magnification below) denotes the KL1–KL2 interface where residues from both α-klotho domains jointly coordinate a Zn^{2+} ion (orange sphere).

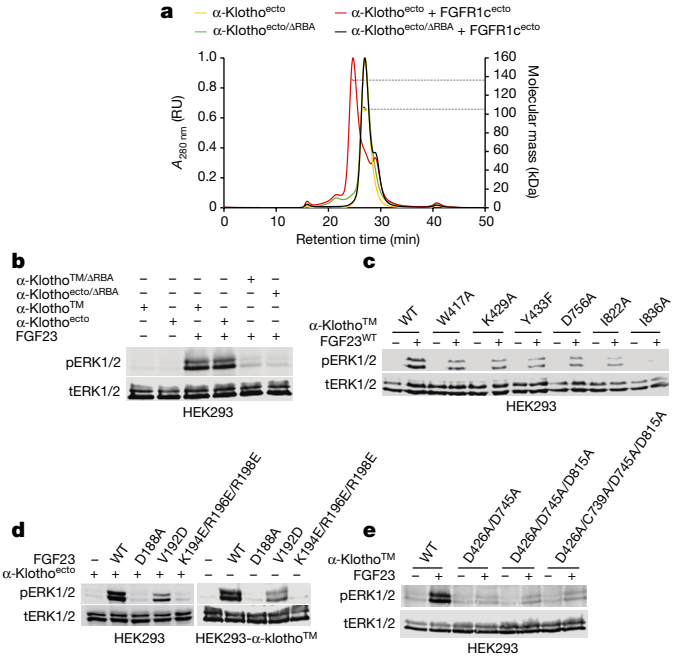

Figure 4 | Mutagenesis experiments validate the crystallographically deduced mode of ternary complex formation. a, Size exclusion chromatography–multi-angle light scattering (SEC–MALS) analysis of FGFR1c^{ecto} interaction with wild-type α-klotho^{ecto} or its RBA deletion mutant. **b**–**e**, Representative immunoblots of phosphorylated ERK (pERK1/2; top) and total ERK (tERK1/2; bottom; sample loading controls) in total HEK293 cell lysates ($n = 3$ independent experiments for each panel). **b**, Analysis of the effects of RBA deletion on the co-receptor activity of α-klotho^{ecto} and α-klotho^{TM} isoforms. **c**, Analysis of mutations in the α-klotho binding pocket that engages the FGF23$^{C\text{-}tail}$. WT, wild type. **d**, Analysis of mutations in the FGF23$^{C\text{-}tail}$ that disrupt α-klotho–FGF23$^{C\text{-}tail}$ interaction. **e**, Analysis of mutations of the four Zn^{2+}-coordinating amino acids in α-klotho.

To test the biological relevance of the observed contacts between α-klotho and the FGF23 C-terminal tail, we introduced several mutations into α-klotho^{TM} and FGF23 to disrupt α-klotho–FGF23 binding (Fig. 4c). Consistent with our structure-based predictions, all α-klotho^{TM} mutants showed an impaired ability to support FGF23 signalling (Fig. 4c). The FGF23 mutants also exhibited a reduced ability to signal, regardless of whether soluble or membrane-bound α-klotho served as co-receptor (Fig. 4d). Remarkably, the FGF23(D188A) mutant (which eliminates the intramolecular hydrogen bonds that support cage conformation) was totally inactive, underscoring the importance of the cage-like conformation in the tethering of FGF23 to α-klotho. Notably, tethering of this cage-like structure requires precise alignment of residues from both KL domains deep within the KL1–KL2 cleft (Fig. 3c), indicating that their correct apposition is critically important for α-klotho co-receptor activity. These structural observations suggest that the bound Zn^{2+} ion serves as a prosthetic group in α-klotho by minimizing interdomain flexibility and hence promoting co-receptor activity. Consistent with such a role, mutants of membrane-anchored α-klotho^{TM} carrying alanine in place of two, three or all four Zn^{2+} coordinating amino acids (Fig. 3c) showed a reduced ability to support FGF23 signalling (Fig. 4e). Together with our data on the effect of RBA deletion, these results corroborate the biological relevance of the crystallographically deduced mode by which α-klotho implements FGF23–FGFR1c proximity and thus confers high binding affinity.

FGF23 signalling is α-klotho- and HS-dependent

Both FGF23 and FGFR1c have a measurable (albeit weak) binding affinity for HS. Because HS is ubiquitously expressed, we wondered whether it participates in the apparent α-klotho^{ecto}-mediated FGF23–FGFR dimerization in our cell-based and *in vivo* experiments. We therefore analysed the molecular mass of the ternary complex in the absence and presence of increasing molar equivalents of homogenously sulfated heparin hexasaccharide (HS6). Consistent with our previous observations, in the absence of HS6, the ternary complex migrated as a monomeric species[10] with an apparent molecular mass of 150 kDa, in good agreement with the theoretical value for a 1:1:1 complex (160 kDa) (Fig. 5a). With increasing molar ratios of HS6 to ternary complex, the peak for monomeric ternary complex diminished, while a new peak with a molecular mass of 300 kDa (corresponding to a 2:2:2 FGF23–FGFR1c^{ecto}–α-klotho^{ecto} dimer) appeared and increased in prominence. Excess HS6 beyond a 1:1 molar ratio of HS6 to ternary complex did not lead to any further increase in the amount of dimer complex formed, as judged by the integrated area of the dimer complex peak (Fig. 5a). We conclude that HS is required for the dimerization of 1:1:1 FGF23–FGFR1c^{ecto}-α-klotho^{ecto} complexes, and that at least a 1:1 molar ratio of HS6 to ternary complex is required for complete dimerization of the complex in solution (Fig. 5a). To confirm the dependency of dimerization on HS, we introduced mutations into the HS-binding sites of FGFR1c (K160Q/K163Q, FGFR1c$^{\Delta HBS}$, and K207Q/R209Q, FGFR1c$^{\Delta HBS'}$) and FGF23 (R140A/R143A, FGF23$^{\Delta HBS}$). Neither mutating the HS-binding site in FGFR1c nor mutating that site in FGF23 affected the formation of a monomeric 1:1:1 FGF23–FGFR1c–α-klotho complex in solution, demonstrating that α-klotho-mediated stabilization of the FGF23–FGFR complex is independent of HS. However, ternary complexes containing any of these three mutants failed to dimerize in the presence of HS6 (Fig. 5b).

Reconstitution experiments in the context of BaF3 cells (an FGFR, α-klotho and HS triple-deficient cell line[29]) showed that both soluble α-klotho^{ecto} and membrane-bound α-klotho^{TM} required HS to support FGF23-mediated FGFR1c activation in a more physiological context (Fig. 5c). We also examined the impact of the HS-binding site mutations in FGFR1c and FGF23 on FGFR1c activation by FGF23 in BaF3 cells (Fig. 5d). In agreement with our solution binding data, activation by FGF23 of HS-binding site mutants of FGFR1c in BaF3 cells was markedly impaired, regardless of whether soluble or membrane-bound α-klotho served as the co-receptor (Fig. 5d). Similarly, the binding site mutant of FGF23 showed a markedly reduced ability to activate FGFR1c (Fig. 5e). These *in vitro* and cell-based analyses unequivocally demonstrate that whereas HS fulfils a dual role in paracrine FGF signalling—enhancing 1:1 FGF–FGFR binding and promoting 2:2 FGF–FGFR dimerization—it shares this task with α-klotho in FGF23 signalling. Thus, α-klotho primarily acts to promote 1:1 FGF23–FGFR1c binding, whereas HS induces the dimerization of the resulting FGF23–FGFR1c–α-klotho complexes.

On the basis of the crystallographically deduced 2:2:2 (Protein Data Bank (PDB) code 1FQ9)[4] and 2:2:1 (PDB code 1E0O)[30] paracrine FGF–FGFR–HS dimerization models, two distinct HS-induced 2:2:2 endocrine FGF23–FGFR1c–α-klotho quaternary dimers can be predicted that differ markedly in the composition of the dimer interface (Extended Data Fig. 8). Specifically, in the 2:2:2:1 model, there would be no protein–protein contacts between the two 1:1:1 FGF23–FGFR1c–α-klotho protomers (Extended Data Fig. 8a). By contrast, in the 2:2:2:2 model, FGF23 and FGFR1c from one 1:1:1 FGF23–FGFR1c–α-klotho protomer would interact with the D2 domain of FGFR1c in the adjacent 1:1:1 FGF23–FGFR1c–α-klotho protomer across a two-fold dimer interface (Extended Data Fig. 8b). On the basis of the fundamental differences in the composition of the dimer interface between these two models, we introduced mutations into the secondary-receptor-binding site (SRBS) in FGF23 (M149A/N150A/P151A; FGF23$^{\Delta SRBS}$) and into the corresponding secondary-ligand-binding site (SLBS) in FGFR1c D2 (I203E, FGFR1c$^{\Delta SLBS}$, and V221D, FGFR1c$^{\Delta SLBS'}$), both of which are unique to the 2:2:2:2 quaternary dimer model. The direct receptor–receptor binding site (RRBS) in FGFR1c D2 (A171D; FGFR1c$^{\Delta RRBS}$), another binding site unique to the 2:2:2:2 model, was also mutated

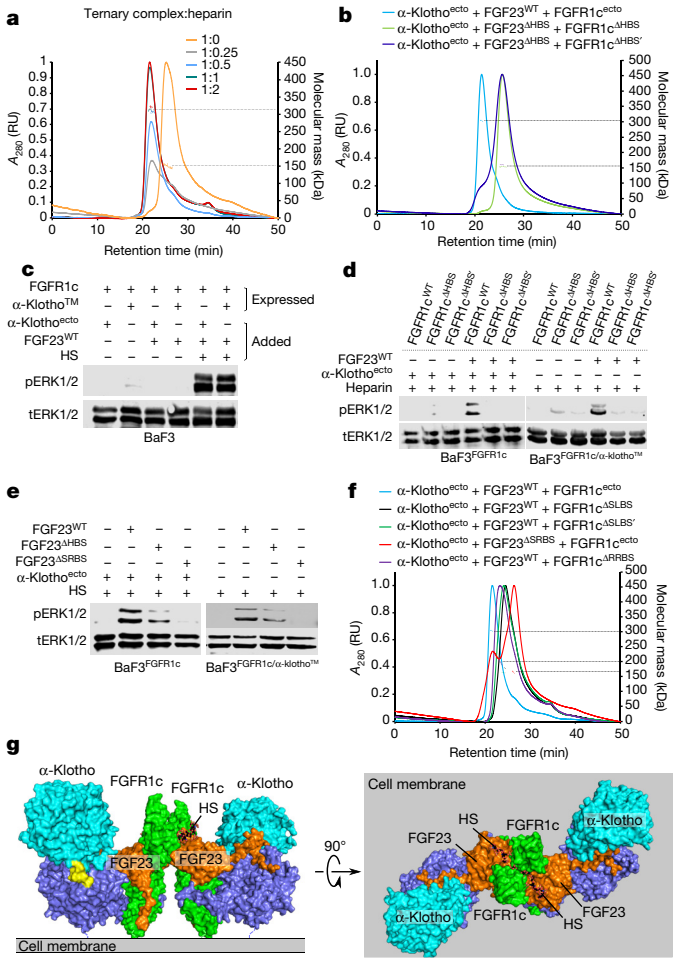

Figure 5 | Heparan sulfate dimerizes two 1:1:1 FGF23–FGFR1c–α-klotho complexes into a symmetric 2:2:2:2 FGF23–FGFR1c–α-klotho–HS signal transduction unit. a, SEC–MALS analysis of the FGF23–FGFR1c^{ecto}–α-klotho^{ecto} complex in the absence or presence of increasing molar amounts of heparin hexasaccharide (HS6). **b**, SEC–MALS analysis of the FGF23–FGFR1c^{ecto}–α-klotho^{ecto} complexes containing HS-binding site mutations of FGF23 and FGFR1c. **c**–**e**, Representative immunoblots of phosphorylated ERK (top) and total ERK (bottom; sample loading controls) in total BaF3 cell lysates ($n = 3$ independent experiments for each panel). **c**, Analysis of HS dependency of FGF23 signalling. **d**, **e**, Analysis of mutations in the HS-binding site of FGFR1c (**d**) and in the HS-binding site or secondary receptor-binding site of FGF23 (**e**). **f**, SEC–MALS analysis of FGF23–FGFR1c^{ecto}–α-klotho^{ecto} complexes containing a secondary receptor-binding site mutation in FGF23, a secondary ligand-binding site mutation in FGFR1c, or a direct receptor–receptor-binding site mutation in FGFR1c. In **b** and **f**, wild-type ternary complex served as controls. **g**, Molecular surface of a 2:2:2:2 FGF23–FGFR1c–α-klotho–HS dimer in two orientations related by a 90° rotation around the horizontal axis: a side-view looking parallel to the plane of a cell membrane (left) and a bird's-eye view looking down onto the plane of a cell membrane (right). HS molecules are shown as black sticks.

(Extended Data Fig. 8b). Although all of these FGF23 and FGFR1c mutants were able to form ternary complexes with α-klotho^{ecto}, the ternary complexes containing any of the mutated proteins were impaired in their ability to dimerize in the presence of HS6 in solution (Fig. 5f). Moreover, the FGF23^{ΔSRBS} mutant showed a markedly diminished ability to activate FGFR1c in BaF3 cells (Fig. 5e). The loss-of-function effects of these mutations are consistent with a 2:2:2:2 quaternary dimer model (Extended Data Fig. 8b). Hence, we envision that HS engages the HS-binding sites of FGFR1c and FGF23 in two stabilized 1:1:1 FGF23–FGFR1c–α-klotho ternary complexes to promote the formation of a two-fold symmetric 2:2:2:2 FGF23–FGFR1c–α-klotho–HS dimer (Fig. 5g). In doing so, HS enhances reciprocal interactions of FGFR1c D2 and FGF23 from one ternary complex with FGFR1c D2 in the other ternary complex, thereby buttressing the dimer (Extended Data Fig. 8b). This replicates the role that HS has in paracrine FGF signalling[4]. In contrast to HS, α-klotho molecules do not directly participate in the dimer interface (Fig. 5g), but rather indirectly support HS-induced dimerization by enhancing 1:1 FGF23–FGFR1c binding affinity. Hence, FGF23 seems to strike a fine balance between losing a large amount of HS-binding affinity to enable its endocrine mode of action and retaining sufficient HS-binding affinity to allow HS-mediated dimerization of two 1:1:1 FGF23–FGFR1c–α-klotho complexes. These considerations do not formally exclude the possibility that 2:2:2:2 and 2:2:2:1 quaternary dimers might co-exist as a higher order cluster on the cell surface, as has been proposed previously for paracrine 2:2:2 and 2:2:1 FGF–FGFR1–HS dimers[31].

FGF19 and FGF21, the other two endocrine FGFs, both require β-klotho as an obligate co-receptor to bind and activate cognate FGFRs[32,33] so as to mediate effects that regulate, for example, metabolic pathways involved in bile acid biosynthesis or fatty acid oxidation[34,35]. On the basis of the structural analysis and supporting cell-based data shown in Extended Data Figs 9 and 10, we propose that β-klotho, similar to α-klotho, functions as a non-enzymatic molecular scaffold to promote signalling by these two FGF hormones.

Online Content Methods, along with any additional Extended Data display items and Source Data, are available in the online version of the paper; references unique to these sections appear only in the online paper.

Received 6 June; accepted 13 December 2017.
Published online 17 January 2018.

1. Shimada, T. *et al.* Targeted ablation of Fgf23 demonstrates an essential physiological role of FGF23 in phosphate and vitamin D metabolism. *J. Clin. Invest.* **113,** 561–568 (2004).
2. Gattineni, J. *et al.* FGF23 decreases renal NaPi-2a and NaPi-2c expression and induces hypophosphatemia *in vivo* predominantly via FGF receptor 1. *Am. J. Physiol. Renal Physiol.* **297,** F282–F291 (2009).
3. Lemmon, M. A. & Schlessinger, J. Cell signaling by receptor tyrosine kinases. *Cell* **141,** 1117–1134 (2010).
4. Schlessinger, J. *et al.* Crystal structure of a ternary FGF-FGFR-heparin complex reveals a dual role for heparin in FGFR binding and dimerization. *Mol. Cell* **6,** 743–750 (2000).
5. Mohammadi, M., Olsen, S. K. & Ibrahimi, O. A. Structural basis for fibroblast growth factor receptor activation. *Cytokine Growth Factor Rev.* **16,** 107–137 (2005).
6. Goetz, R. & Mohammadi, M. Exploring mechanisms of FGF signalling through the lens of structural biology. *Nat. Rev. Mol. Cell Biol.* **14,** 166–180 (2013).
7. Kuro-o, M. *et al.* Mutation of the mouse klotho gene leads to a syndrome resembling ageing. *Nature* **390,** 45–51 (1997).
8. Henrissat, B. & Davies, G. Structural and sequence-based classification of glycoside hydrolases. *Curr. Opin. Struct. Biol.* **7,** 637–644 (1997).
9. Goetz, R. *et al.* Klotho coreceptors inhibit signaling by paracrine fibroblast growth factor 8 subfamily ligands. *Mol. Cell. Biol.* **32,** 1944–1954 (2012).
10. Goetz, R. *et al.* Isolated C-terminal tail of FGF23 alleviates hypophosphatemia by inhibiting FGF23–FGFR–Klotho complex formation. *Proc. Natl Acad. Sci. USA* **107,** 407–412 (2010).
11. Urakawa, I. *et al.* Klotho converts canonical FGF receptor into a specific receptor for FGF23. *Nature* **444,** 770–774 (2006).
12. Kurosu, H. *et al.* Regulation of fibroblast growth factor-23 signaling by klotho. *J. Biol. Chem.* **281,** 6120–6123 (2006).
13. Li, S. A. *et al.* Immunohistochemical localization of Klotho protein in brain, kidney, and reproductive organs of mice. *Cell Struct. Funct.* **29,** 91–99 (2004).
14. van Loon, E. P. *et al.* Shedding of klotho by ADAMs in the kidney. *Am. J. Physiol. Renal Physiol.* **309,** F359–F368 (2015).
15. Lindberg, K. *et al.* The kidney is the principal organ mediating klotho effects. *J. Am. Soc. Nephrol.* **25,** 2169–2175 (2014).
16. Chen, C. D., Podvin, S., Gillespie, E., Leeman, S. E. & Abraham, C. R. Insulin stimulates the cleavage and release of the extracellular domain of Klotho by ADAM10 and ADAM17. *Proc. Natl Acad. Sci. USA* **104,** 19796–19801 (2007).
17. Imura, A. *et al.* Secreted Klotho protein in sera and CSF: implication for post-translational cleavage in release of Klotho protein from cell membrane. *FEBS Lett.* **565,** 143–147 (2004).
18. Matsumura, Y. *et al.* Identification of the human klotho gene and its two transcripts encoding membrane and secreted klotho protein. *Biochem. Biophys. Res. Commun.* **242,** 626–630 (1998).
19. Shiraki-Iida, T. *et al.* Structure of the mouse klotho gene and its two transcripts encoding membrane and secreted protein. *FEBS Lett.* **424,** 6–10 (1998).

20. Kurosu, H. *et al.* Suppression of aging in mice by the hormone Klotho. *Science* **309,** 1829–1833 (2005).
21. Hu, M. C., Shiizaki, K., Kuro-o, M. & Moe, O. W. Fibroblast growth factor 23 and Klotho: physiology and pathophysiology of an endocrine network of mineral metabolism. *Annu. Rev. Physiol.* **75,** 503–533 (2013).
22. Chang, Q. *et al.* The β-glucuronidase klotho hydrolyzes and activates the TRPV5 channel. *Science* **310,** 490–493 (2005).
23. Cha, S. K. *et al.* Removal of sialic acid involving Klotho causes cell-surface retention of TRPV5 channel via binding to galectin-1. *Proc. Natl Acad. Sci. USA* **105,** 9805–9810 (2008).
24. Hu, M. C. *et al.* Klotho: a novel phosphaturic substance acting as an autocrine enzyme in the renal proximal tubule. *FASEB J.* **24,** 3438–3450 (2010).
25. Imura, A. *et al.* α-Klotho as a regulator of calcium homeostasis. *Science* **316,** 1615–1618 (2007).
26. Hayashi, Y. *et al.* Klotho-related protein is a novel cytosolic neutral beta-glycosylceramidase. *J. Biol. Chem.* **282,** 30889–30900 (2007).
27. Andrukhova, O. *et al.* Klotho lacks an FGF23-independent role in mineral homeostasis. *J. Bone Miner. Res.* **32,** 2049–2061 (2017).
28. Wu, X. *et al.* C-terminal tail of FGF19 determines its specificity toward Klotho co-receptors. *J. Biol. Chem.* **283,** 33304–33309 (2008).
29. Ornitz, D. M. *et al.* Heparin is required for cell-free binding of basic fibroblast growth factor to a soluble receptor and for mitogenesis in whole cells. *Mol. Cell. Biol.* **12,** 240–247 (1992).
30. Pellegrini, L., Burke, D. F., von Delft, F., Mulloy, B. & Blundell, T. L. Crystal structure of fibroblast growth factor receptor ectodomain bound to ligand and heparin. *Nature* **407,** 1029–1034 (2000).
31. Harmer, N. J. *et al.* Towards a resolution of the stoichiometry of the fibroblast growth factor (FGF)–FGF receptor–heparin complex. *J. Mol. Biol.* **339,** 821–834 (2004).
32. Ogawa, Y. *et al.* βKlotho is required for metabolic activity of fibroblast growth factor 21. *Proc. Natl Acad. Sci. USA* **104,** 7432–7437 (2007).
33. Kurosu, H. *et al.* Tissue-specific expression of βKlotho and fibroblast growth factor (FGF) receptor isoforms determines metabolic activity of FGF19 and FGF21. *J. Biol. Chem.* **282,** 26687–26695 (2007).
34. Holt, J. A. *et al.* Definition of a novel growth factor-dependent signal cascade for the suppression of bile acid biosynthesis. *Genes Dev.* **17,** 1581–1591 (2003).
35. Potthoff, M. J. *et al.* FGF21 induces PGC-1alpha and regulates carbohydrate and fatty acid metabolism during the adaptive starvation response. *Proc. Natl Acad. Sci. USA* **106,** 10853–10858 (2009).
36. Pitteloud, N. *et al.* Digenic mutations account for variable phenotypes in idiopathic hypogonadotropic hypogonadism. *J. Clin. Invest.* **117,** 457–463 (2007).

Supplementary Information is available in the online version of the paper.

Acknowledgements We thank N. J. Cowan for critically reading and editing the manuscript, and C.-S. Huang for help with diffraction data processing with XDS. This work was primarily supported by NIH grant R01 DE13686 (to M.M.). Support was also provided by National Key R&D Program of China (#2017YFA0506000 to X.L.). Funding for mouse studies was provided by R01 DK092461, P30 DK079328 (to O.W.M.), and R01 DK091392 (to M.C.H). Beamlines at the Northeastern Collaborative Access Team (NE-CAT) facility at the Advanced Photon Source of Argonne National Laboratory are primarily funded by NIH NIGMS and member institutions.

Author Contributions G.C. purified and crystallized the ternary complex, analysed the crystal structure, generated SEC–MALS data (Figs 4a, 5a, b, f), cell-based data (Fig. 4), enzyme and thermostability assay data (Fig. 2c), and participated in the design of experiments and the writing/revising of the manuscript. Y.L. helped with data collection and analysis of the crystal structure, generated cell-based data (Fig. 5), and participated in manuscript revision. R.G. established expression and purification protocols for the ternary complex, performed ternary complex characterization, analysed mouse data, and participated in editing and revising the manuscript. L.F. generated expression constructs for FGF23, FGFR1c^{ecto}, α-klotho^{ecto} and their structure-based mutated forms, and helped with ternary complex purification. S.J. assisted with diffraction data collection and performed excitation/emission scanning of the FGF23–FGFR1c^{ecto}–α-klotho^{ecto} crystal (Extended Data Fig. 2c). M.-C.H. and O.W.M. generated the mouse data (Extended Data Figs 1c, d and 7a, b). G.L. and X.L. (mentors of G.C. and L.F.) participated in manuscript revision. M.M. developed and directed the project, solved, refined, analysed and interpreted the crystal structure of the ternary complex, and wrote the manuscript.

Author Information Reprints and permissions information is available at www.nature.com/reprints. The authors declare competing financial interests: details are available in the online version of the paper. Readers are welcome to comment on the online version of the paper. Publisher's note: Springer Nature remains neutral with regard to jurisdictional claims in published maps and institutional affiliations. Correspondence and requests for materials should be addressed to M.M. (moosa.mohammadi@nyumc.org) or X.L. (xiaokunli@wzmu.edu.cn).

Reviewer Information *Nature* thanks M. Kuro-o and the other anonymous reviewer(s) for their contribution to the peer review of this work.

METHODS

No statistical methods were used to predetermine sample size. The experiments were not randomized and, except for the data shown in Extended Data Fig. 7a, b, investigators were not blinded to allocation during experiments and outcome assessment.

DNA expression constructs. cDNA fragments encoding full-length human α-klotho, β-klotho and FGFR1c were amplified by PCR and subcloned into the lentiviral transfer plasmids pEF1α-IRES-hygro (α-/β-klotho) or pEF1α-IRES-Neo (FGFR1c) using a ligation-independent In-Fusion HD cloning kit (639648, Clontech Laboratories). PCR primers for *FGFR1* 'c' isotype were designed using NEBaseChanger software version 1.2.6 (New England Biolabs) and primers for *KL* and *KLB* (encoding α-klotho and β-klotho, respectively) were designed using the primer design tool for the In-Fusion HD cloning kit (Clontech Laboratories). A cDNA fragment encoding the entire extracellular domain of human α-klotho (residues Met1 to Ser981; α-klotho^{ecto}) was subcloned into the mammalian expression plasmid pEF1α/myc-His A. DNA fragments for the mature form (that is, without the signal sequence) of human FGF23 (residues Tyr25 to Ile251), human FGF21 (residues His29 to Ser209), and the extracellular D2–D3 region of human FGFR1c (residues Asp142 to Arg365; FGFR1c^{ecto}), which is both necessary and sufficient for FGF binding, were amplified by PCR and ligated into the cloning sites of the bacterial expression plasmids pET-30a and pET-28a, respectively. Single/multiple site mutations, loop deletions and truncations were introduced into expression constructs encoding the wild-type proteins using a Q5 Site-Directed Mutagenesis Kit (E0554S, New England Biolabs). The integrity of each expression construct was confirmed by restriction enzyme digestion and DNA sequencing. Information on the constructs is provided in the Supplementary Tables 1 and 2.

Recombinant protein expression and purification. *N*-acetylglucosaminyltransferase I (GnTI) deficient HEK293S cells (CRL-3022, American Type Culture Collection (ATCC)) were transfected by calcium phosphate co-precipitation with the expression construct encoding α-klotho^{ecto}. G418-resistant colonies were selected for α-klotho^{ecto} expression using 0.5 mg ml^{-1} G418 (6483, KSE Scientific). The clone with the highest expression level was propagated in DME/F12 medium (SH30023.02, HyClone) supplemented with 10% fetal bovine serum (FBS) (35-010-CV, CORNING), 100 U ml^{-1} penicillin plus 100 μg ml^{-1} streptomycin (15140-122, Gibco), and 0.5 mg ml^{-1} G418. For protein production, 1×10^6 cells were seeded in 25 cm cell culture dishes in 20 ml DME/F12 medium containing 10% FBS and grown for 24 h. Thereafter, the medium was replaced with 25 ml DME/F12 medium containing 1% FBS. Three days later, secreted α-klotho^{ecto} from two litres of conditioned medium was captured on a 5 ml heparin affinity HiTrap column (GE Healthcare) and eluted with a 100 ml linear NaCl gradient (0–1.0 M). Column fractions containing α-klotho^{ecto} were pooled and diluted tenfold with 25 mM Tris pH 8.0 buffer, and the diluted protein sample was loaded onto an anion exchange column (SOUCRE Q, GE Healthcare) and eluted with a 280 ml linear NaCl gradient (0–0.4 M). As a final purification step, SOURCE Q fractions containing α-klotho^{ecto} were concentrated and applied to a Superdex 200 column (GE Healthcare). α-Klotho^{ecto} protein was eluted isocratically in 25 mM HEPES pH 7.5 buffer containing 500 mM NaCl and 100 mM $(NH_4)_2SO_4$. A mutant of α-klotho^{ecto} lacking the receptor binding arm (α-klotho$^{ecto/\Delta RBA}$) was expressed and purified similarly as the wild-type counterpart.

Human wild-type FGF23 and its mutants were expressed in *Escherichia coli* BL21 DE3 cells. Inclusion bodies enriched in misfolded insoluble FGF23 protein were dissolved in 6 M guanidinium hydrochloride and FGF23 proteins were refolded by dialysis for 2 days at 4 °C against buffer A (25 mM HEPES pH 7.5, 150 mM NaCl, 7.5% glycerol) followed by buffer B (25 mM HEPES pH 7.5, 100 mM NaCl, 5% glycerol). Correctly folded FGF23 proteins were captured on a 5 ml heparin affinity HiTrap column (GE Healthcare) and eluted with a 100 ml linear NaCl gradient (0–2.0 M). Final purification of FGF23 proteins was achieved by cation exchange chromatography (SOURCE S, GE Healthcare) with a 280 ml linear NaCl gradient (0–0.4 M). Human FGFR1c^{ecto} and its mutants were also expressed as inclusion bodies in *E. coli* BL21 DE3 and refolded *in vitro* by slow dialysis at 4 °C against the following buffers: buffer A (25 mM Tris pH 8.2, 150 mM NaCl, 7.5% glycerol), buffer B (25 mM Tris pH 8.2, 100 mM NaCl, 5% glycerol), and buffer C (25 mM Tris pH 8.2, 50 mM NaCl, 5% glycerol); dialysis against each buffer was for minimally 12 h. Properly folded FGFR1c proteins were purified by heparin affinity chromatography followed by size-exclusion chromatography as described above. All column chromatography was performed at 4 °C on an AKTA pure 25 l system (GE Healthcare).

Crystallization and X-ray crystal structure determination. To facilitate crystallization of the FGF23–FGFR1c^{ecto}–α-klotho^{ecto} complex, we used a proteolytically and structurally more stable FGF23 protein variant, which lacked 46 residues from the FGF23 C-terminus (Cys206 to Ile251) and carried Arg-to-Gln mutations at positions 176 and 179 of the 176-Arg-His-Thr-Arg-179 proteolytic cleavage motif in FGF23. The Arg-to-Gln mutations occur naturally in patients with autosomal dominant hypophosphatemic rickets (ADHR)[37], and deletion of C-terminal residues Cys206 to Ile251 has no effect on the phosphaturic activity of FGF23 in mice or its signalling potential in α-klotho^{TM}-expressing cultured cells[10]. Thus, the first 26 amino acids (Ser180 to Ser205) of the 72-amino-acid-long C-terminal tail of FGF23, defined as the region past the 176-Arg-His-Thr-Arg-179 proteolytic cleavage site, comprise the minimal region of the FGF23 C-terminal tail for binding the FGFR1c^{ecto}–α-klotho^{ecto} complex[10]. To prepare the FGF23–FGFR1c^{ecto}–α-klotho^{ecto} complex, its purified components were mixed at a molar ratio of 1.2:1.2:1 and spin-concentrated using an Amicon Ultra-15 concentrator (UFC901024, Merck Millipore). The concentrated sample was applied to a Superdex 200 column (GE Healthcare) and eluted isocratically in 25 mM HEPES pH 7.5 buffer containing 500 mM NaCl and 100 mM $(NH_4)_2SO_4$. Column peak fractions were analysed by SDS–PAGE and peak fractions containing the ternary complex were concentrated to 7 mg ml^{-1}. Concentrated ternary complex was screened for crystallization by sitting drop vapour diffusion. A range of commercially available crystallization screen kits was used: Protein Complex Suite (130715), Classics Suite (130701), Classics II Suite (130723), and Classics Lite Suite (130702) from Qiagen; Crystal Screen (HR2-110), Crystal Screen 2 (HR2-112), Crystal Screen Lite (HR2-128), PEG/Ion Screen (HR2-126), and PEGRx1 (HR2-082) from Hampton Research; and PEG Grid Screening Kit (36436) and Crystallization Cryo Kit (75403) from Sigma-Aldrich. Drops consisting of 100 nl reservoir solution and 100 nl protein complex solution were equilibrated against 100 μl well volume set up in 96-well plates (Fisher Scientific) using a Mosquito crystallization robot (TTP Labtech). Plates were stored at 18 °C and automatically imaged by Rock Imager 1000 (Formulatrix). Image data were collected and managed using Rock Maker software version 3.1.4.0 (Formulatrix). One crystal hit was obtained after 7 days of plate incubation at 18 °C and one crystallization condition from the Protein Complex Suite (130715, Qiagen) was chosen for optimization using the Additive Screen (HR2-428) from Hampton Research. Crystals were confirmed as protein crystals by UV imaging using Rock Imager 1000 (Formulatrix). Crystal growth in optimized conditions was scaled up in 24-well VDXm plates (Hampton Research) where crystals were grown by hanging drop vapour diffusion. Larger crystals ($80 \times 76 \times 35$ μm) were obtained within 28 days by mixing 1 μl of protein complex and 1 μl of crystallization solution. Some of those crystals were dissolved in Lämmli sample buffer after thorough rinsing, and analysed by SDS–PAGE and staining with Coomassie blue to confirm the presence of all three proteins in the ternary complex.

Crystals of ternary complex were briefly soaked in cryo-protective solution consisting of mother liquor supplemented with 25% (w/v) glycerol. These were then mounted on CryoLoops (Hampton Research) and flash-frozen in liquid nitrogen. Crystal screening for X-ray diffraction and diffraction data collection were performed at 100 K on one of the NE-CAT beam lines at the Advanced Photon Source synchrotron of Argonne National Laboratory. X-ray images were recorded with an ADSC Quantum 315 CCD detector with primary oscillations at 100 K, a wavelength of 0.97918 Å, and a crystal-to-detector distance of 420 mm. Crystals of the ternary complex belong to the monoclinic space group *C*2, and contain one ternary complex molecule in the asymmetric unit. X-ray diffraction data sets were collected to 3.0 Å from native protein crystals, integrated, and scaled using XDS[38] and SCALA[39] from the *CCP*4 software suite[40].

A clear molecular replacement solution was found for both KL domains using the Phaser module of PHENIX[41] and homology models of KL1 and KL2, which were built with Rosetta software available through the ROBETTA Protein Structure Prediction Server (http://robetta.bakerlab.org). However, the FGF23–FGFR1c component of the ternary complex could not be found even after fixing the coordinates of the partial solution found for the KL domains. Through careful inspection of the crystal lattice and the $F_o - F_c$ difference and $2F_o - F_c$ composite maps generated using the partial model, we succeeded in manually placing an FGF23–FGFR1c D2 portion of the FGF23–FGFR1c complex. This was created using the experimental crystal structures of SOS-bound FGF23[42] (PDB code 2P39) and the FGF2-bound FGFR1c ectodomain[43] (PDB code 1CVS). After a few rounds of refinements, FGFR1c D3 could also be placed manually. Iterative rounds of model building and refinement were carried out using Coot[44] and the Phenix.Refine module of PHENIX[41].

The structure has been refined to 3.0 Å resolution with working and free *R*-factors of 23.46 and 28.26%, respectively, and good Ramachandran plot statistics. X-ray diffraction data collection and structure refinement statistics are summarized in Extended Data Table 1. The final model comprises residues Glu34 to His977 of human α-klotho^{ecto}, residues Met149 to Ala361 of human FGFR1c^{ecto} and residues Tyr25 to Thr200 of human FGF23. Owing to insufficient electron density, the following residues of the ternary complex could not be built: 1) Leu98 to Ser115 (β1α1 loop) of α-klotho^{ecto} KL1, 2) Glu957 to Glu960 (an ADAM protease cleavage site) at the junction between the rigid core of α-klotho^{ecto} KL2 and the flexible extracellular juxtamembrane linker that connects KL2 to the transmem-

brane helix of α-klotho, 3) the last four residues of the extracellular juxtamembrane linker (Thr978 to Ser981) of α-klotho^{ecto}, 4) the last five C-terminal residues of FGF23 (Pro201 to Ser205), 5) Asp142 to Arg148 N-terminal to the D2 domain of FGFR1c^{ecto}, and 6) Leu362 to Arg365 C-terminal to the D3 domain of FGFR1c^{ecto}. Ordering of the first six N-terminal residues of FGF23 (Tyr25 to Pro30) is influenced by crystal lattice contacts.

SEC–MALS. The SEC–MALS instrument setup consisted of a Waters Breeze 2 HPLC system (Waters), a miniDAWN-TREOS 18-angle static light scattering detector with built-in 658.0-nm wavelength laser (Wyatt Technology Corp.), and an Optilab rEX refractive index detector (Wyatt Technology Corp.). A Superdex 200 10/300 GL column (GE Healthcare) was placed in-line between the HPLC pump (Waters 1525) and the HPLC UV (Waters 2998 Photodiode Array), laser light scattering, and refractive index detectors. Light scattering and refractive index detectors were calibrated following the manufacturer's guidelines. The refractive index increment (dn/dc), in which n is the refractive index and c is the concentration of the mixture of DDM and CHS in 20 mM Tris-HCl pH 8.0 buffer containing 300 mM NaCl, was determined offline using an Optilab T-rEX refractive index detector. Monomeric bovine serum albumin (23210, Thermo Scientific) was used as part of routine data quality control.

At least 60 ml of 25 mM HEPES pH 7.5 buffer containing 150 mM NaCl were passed through the system at a flow rate of 0.5 ml min^{-1} to equilibrate the Superdex 200 10/300 GL column and establish stable baselines for light scattering and refractive index detectors. Purified α-klotho^{ecto}, FGFR1c^{ecto} (wild type or mutant), and FGF23 (wild type or mutant) proteins were mixed at a molar ratio of 1:1:1 and concentrated to 12.5 μM. Protein samples (50 μl) with a molar equivalent of a heparin hexasaccharide (HO06, Iduron) were injected onto the gel filtration column, and the column eluent was continuously monitored for 280 nm absorbance, laser light scattering, and refractive index. In a separate set of experiments, 50 μl of 1:1:1 FGF23–FGFR1c^{ecto}–α-klotho^{ecto} ternary complex at 12.5 μM concentration was mixed with heparin hexasaccharide at molar ratios of 1:0.25, 1:0.5, 1:1 or 1:2, and the mixtures were injected onto the gel filtration column. As a control, 50 μl of ternary complex without added heparin hexasaccharide were run on the column. In yet another set of experiments, α-klotho^{ecto} (wild type or mutant) and FGFR1c^{ecto} were mixed at a molar ratio of 1:1, and 50 μl of concentrated protein mixtures were injected onto the gel filtration column. 50 μl of concentrated α-klotho^{ecto} (wild type or mutant) alone were run as a control in these experiments. The analyses were performed at ambient temperature. Data were collected every second at a flow rate of 0.5 ml min^{-1}. Laser light scattering intensity and eluent refractive index (concentration) data were adjusted manually for the volume delay of UV absorbance at 280 nm, and were processed using ASTRA software (Wyatt Technology Corp.). A protein refractive index increment (dn/dc value) of 0.185 ml g^{-1} was used for molecular mass calculations.

Cell line culture and stimulation and analysis of protein phosphorylation. HEK293 cells (a gift from A. Mansukhani, identified by morphology check under microscope, mycoplasma negative in DAPI) were maintained in DMEM medium (10-017-CV, CORNING) supplemented with 10% FBS, 100 U ml^{-1} of penicillin and 100 μg ml^{-1} streptomycin. HEK293 cells naturally express multiple FGFR isoforms including FGFR1c, FGFR3c and FGFR4, but lack α-klotho or β-klotho co-receptors. BaF3 cells (a gift from S. Byron, identified by morphology check under microscope, mycoplasma negative in DAPI), an IL-3-dependent haematopoietic pro B cell line, were cultured in RPMI 1640 medium (10-040-CV, CORNING) supplemented with 10% FBS, 100 U ml^{-1} of penicillin, 100 μg ml^{-1} streptomycin and 5 ng ml^{-1} mouse IL-3 (#GFM1, Cell Guidance Systems). BaF3 cells do not express FGFRs, α-/β-klotho co-receptors, or HS cofactors, and hence are naturally non-responsive to FGFs. However, via controlled ectopic expression of FGFRs and klotho co-receptors and exogenous supplementation with soluble HS, these cells can be forced to respond to FGF stimulation. As such, the BaF3 cell line has served as a powerful tool for reconstituting FGF–FGFR cell surface signal transduction complexes to dissect the molecular mechanisms of paracrine and endocrine FGF signalling[29,45,46].

Stable or transient expression of full-length (transmembrane) human α-klotho, β-klotho, FGFR1c, and mutants of these proteins in HEK293 or BaF3 cells was achieved using lentiviral vectors. To generate lentiviral expression vectors, HEK293 cells were seeded at a density of about 8×10^5 in 10 cm cell culture dishes and co-transfected by calcium phosphate co-precipitation with 8 μg of lentiviral transfer plasmid encoding wild-type or mutant α-klotho, β-klotho or FGFR1c, 1.6 μg of pMD2.G envelope plasmid, and 2.5 μg of psPAX2 packaging plasmid. Fresh medium was added to the cells for a 3-day period after transfection. Cell culture supernatant containing recombinant lentivirus particles was collected and used to infect 2×10^5 HEK293 or BaF3 cells in the presence of polybrene (5 μg ml^{-1}; 134220, Santa Cruz Biotechnology). Stable transfectants were selected using hygromycin (1 mg ml^{-1}, ant-hg-1, InvivoGen) or G418 (0.5 mg ml^{-1}, 6483, KSE Scientific). For transient protein expression, 2×10^5 HEK293 cells were plated in 6-well cell culture dishes and on the following day, the cells were infected with recombinant lentivirus in the presence of polybrene (16 μg).

For cell stimulation studies, unmodified and stably transfected HEK293 cells were seeded in 6-well cell culture plates at a density of 4×10^5 cells per well and maintained for 24 h in cell culture medium without FBS. In the case of transiently transfected HEK293 cells, medium containing lentivirus particles was removed from the cells after incubation for approximately 12 h, and the cells were also serum-starved for 24 h. Stably transfected BaF3 cells were seeded in 10 cm cell culture dishes at a density of 6×10^6 cells and serum-starved for 6 h. Unmodified HEK293 cells were stimulated for 10 min with wild-type or mutant FGF23 both in the presence and absence of wild-type or mutant α-klotho^{ecto}. HEK293 cells stably or transiently expressing wild-type α-klotho^{TM} or its mutants were stimulated with wild-type or mutant FGF23 alone. In one set of experiments, HEK293 cells expressing wild-type α-klotho^{TM} were pretreated with α-klotho^{ecto} for 10 min before stimulation with wild-type FGF23. BaF3 cells expressing wild-type or mutant FGFR1c were stimulated with wild-type or mutant FGF23 in the presence or absence of α-klotho^{ecto} and heparin. BaF3 cells co-expressing wild-type α-klotho^{TM} and wild-type or mutant FGFR1c were stimulated with wild-type or mutant FGF23 in the presence of heparin. BaF3 cells co-expressing wild-type FGFR1c and wild-type or mutant β-klotho^{TM} were stimulated with wild-type FGF21 in the presence or absence of heparin.

After stimulation, cells were lysed, and lysate samples containing approximately 30 μg total cellular protein were electrophoresed on 12% SDS–PAGE and electrotransferred onto a nitrocellulose membrane. The membrane was blocked for 1 h at ambient temperature in Tris-buffered saline pH 7.6 containing 0.05% Tween-20 and 5% BSA (BP1600-100, Fisher BioReagents). Rabbit monoclonal antibodies to phosphorylated ERK1/2 (4370, Cell Signaling Technology) and total (phosphorylated and unphosphorylated) ERK1/2 (4695, Cell Signaling Technology) were diluted 1:2,000 and 1:1,000, respectively, in blocking buffer. After overnight incubation at 4 °C with one of these diluted antibodies, the blot was washed with Tris-buffered saline pH 7.6 containing 0.05% Tween-20, and then incubated at ambient temperature for 30 min with 1:10,000-diluted IRDye secondary antibody (926-32211 (goat anti-rabbit), LI-COR). After another round of washing with Tris-buffered saline pH 7.6 containing 0.05% Tween-20, the blot was imaged on an Odyssey Fc Dual-mode Imaging System (LI-COR).

α-Klotho treatment of mice and serum, urinary phosphate analysis. Mice of the strain 129/Sv (Charles River Laboratories) were housed in a room with a temperature of 22 ± 1 °C and a 12 h:12 h light/dark cycle, and had ad libitum access to tap water and Teklad global 16% rodent diet (Envigo). Ten female and ten male 6-week-old mice of each gender were assigned to receive either recombinant α-klotho^{ecto} protein diluted in isotonic saline (0.1 mg kg^{-1} body weight) or protein diluent only (buffer control). Mice were placed in metabolic cages for a one-day acclimation, and returned to the cages for 24-h urine collection after intraperitoneal injection of α-klotho^{ecto} protein or buffer control. After urine collection, mice were placed under isofluorane anaesthesia, and blood was drawn from the retro-orbital sinus and transferred into tubes containing a few drops of sterile solution of heparin (Sagent Pharmaceuticals). After centrifugation at 3,000g at 4 °C for 5 min, supernatant plasma was taken out of the tubes and stored at −80 °C. Blood and urine samples were also collected before injection of α-klotho^{ecto} or buffer control. Phosphate and creatinine concentrations in plasma and urine were measured using a Vitros Chemistry Analyzer (Ortho-Clinical Diagnosis) and a P/ACE MDQ Capillary Electrophoresis System equipped with a photodiode detector (Beckman-Coulter), respectively. The Mouse Metabolic Phenotyping Core Facility at UT Southwestern Medical Center carried out the measurements of these analytes.

In a separate set of experiments, 10- to 12-week-old mice were given an intraperitoneal injection of wild-type α-klotho^{ecto} (0.1 mg kg^{-1} body weight), RBA deletion mutant, α-klotho$^{ecto/\Delta RBA}$ (0.1 mg kg^{-1} body weight), or protein diluent only (three female and three male mice per group), and blood and urine samples were collected for measurement of phosphate and creatinine as described above. In yet another set of experiments, 10- to 12-week-old mice were injected intraperitoneally with 0.1 mg kg^{-1} body weight of wild-type α-klotho^{ecto} (two female and one male mice), mutant α-klotho$^{ecto/\Delta RBA}$ (two female and two male mice), or protein diluent only (two female and one male mice), and kidneys were obtained from the mice under isofluorane anaesthesia four hours after the injection. Total RNA was extracted from the kidneys using RNAeasy kit (Qiagen), and *Egr1* mRNA levels were quantified by quantitative PCR (qPCR) with cyclophilin (also known as *Ppia*) as a control. Template cDNA for the PCR was generated using SuperScript III First Strand Synthesis System (Invitrogen) and oligo-(dT) primers. PCR primers for *Egr1* were 5′-GAGGAGATGATGCTGCTGAG-3′ and 5′-TGCTGCTGCTGCTATTACC-3′. PCR primers for cyclophilin were 5′-GTCTCTTTTCGCCGCTTGCT-3′ and 5′-TCTGCTGTCTTTGGAACTTTGTCTG-3′. qPCR was performed in

triplicate for each kidney RNA sample. Except for Egr1 expression analysis, data were analysed by paired Student's *t*-test. All studies in mice were approved by the Institutional Animal Care and Use Committee at the University of Texas Southwestern Medical Center and conducted following the National Institutes of Health Guide for the Care and Use of Laboratory Animals.

Enzymatic assay. To examine α-klotho^{ecto} for glycoside-hydrolase activity, 4-methylumbelliferyl-β-D-xylopyranoside (M7008, Sigma-Aldrich), 4-methylumbelliferyl-β-D-glucuronide (474427, Sigma-Aldrich) and 4-methylumbelliferyl-α-D-*N*-acetylneuraminic acid (69587, Sigma-Aldrich) were selected as substrates and commercially available recombinant neuraminidase (#10269611001, Roche Diagnostics GmbH) and β-Glucuronidase (#G0251, Sigma-Aldrich) were used as positive controls. 20 μg of α-klotho^{ecto} or the control enzymes were added into reaction buffer (0.1 M sodium citrate buffer, pH 5.6, 0.05 M NaCl, 0.01% Tween 20) containing 0.5 mM substrate at a final volume of 100 μl, and the reaction mixtures were incubated at 37 °C for 2 h. Enzymatic activity was assessed by quantifying fluorescence intensity of released 4-methylumbelliferone at an excitation wavelength of 360 nm and an emission wavelength of 450 nm using a FlexStation 3 Multi-Mode Microplate Reader (Molecular Devices).

Fluorescence dye-based thermal shift assay. SYPRO Orange dye (S6650, ThermoFisher Scientific) was used as the fluorescent probe. 15 μl of 20 μM solutions of protein samples (wild-type and mutated forms of FGF23; α-klotho^{ecto} or α-klotho$^{ecto/\Delta RBA}$ alone; 1:1 mixtures of α-klotho^{ecto} or α-klotho$^{ecto/\Delta RBA}$ with FGF23 C-terminal tail peptide) were mixed with 5 μl of working dye solution (1:25 dilution) in duplicate in PCR strips. A temperature gradient from 4 °C to 100 °C, at 1 °C per min increment was carried out with a CFX96 Touch Real-Time PCR Detection System (Bio-Rad). Fluorescence was recorded as a function of temperature in real time. The melting temperature (T_m) was calculated with StepOne software v2.2 as the maximum of the derivative of the resulting SYPRO Orange fluorescence curves.

Statistics and reproducibility. Glycoside-hydrolase activity of α-klotho^{ecto}, neuraminidase and β-glucuronidase was measured in triplicate; one triplicate representative of three independent experiments is shown in Fig. 2c. Each set of immunoblot experiments (data shown in Figs 4b–e, 5c–e and Extended Data Figs 1b, 4c, 7e and 10b, c) was independently repeated three times. Renal mRNA levels of mouse *Egr1* and cyclophilin were each measured in triplicate, and mean values of relative *Egr1* mRNA concentrations from three independent samples for buffer control, three independent samples for α-klotho^{ecto} treatment, and four independent samples for α-klotho$^{ecto/\Delta RBA}$ treatment are shown in Extended Data Figs 1d and 7b, respectively. Protein elution profiles from size-exclusion columns shown in Figs 4a, 5a, b, f and Extended Data Fig. 7c are each representative of three independent experiments.

Data availability. Atomic coordinates and structure factors for the crystal structure of the FGF23–FGFR1c^{ecto}–α-klotho^{ecto} ternary complex are accessible at the RCBS Protein Data Bank (PDB) under accession code 5W21. Requests for *in vivo* datasets should be directed to O.W.M. Requests for all other reagents and datasets, including recombinant proteins, engineered cell lines and cell-based data, should be made to M.M.

37. White, K. E. *et al.* Autosomal dominant hypophosphataemic rickets is associated with mutations in *FGF23*. *Nat. Genet.* **26,** 345–348 (2000).
38. Kabsch, W. Xds. *Acta Crystallogr. D* **66,** 125–132 (2010).
39. Evans, P. Scaling and assessment of data quality. *Acta Crystallogr. D* **62,** 72–82 (2006).
40. Winn, M. D. *et al.* Overview of the *CCP*4 suite and current developments. *Acta Crystallogr. D* **67,** 235–242 (2011).
41. Adams, P. D. *et al.* PHENIX: a comprehensive Python-based system for macromolecular structure solution. *Acta Crystallogr. D* **66,** 213–221 (2010).
42. Goetz, R. *et al.* Molecular insights into the klotho-dependent, endocrine mode of action of fibroblast growth factor 19 subfamily members. *Mol. Cell. Biol.* **27,** 3417–3428 (2007).
43. Plotnikov, A. N., Schlessinger, J., Hubbard, S. R. & Mohammadi, M. Structural basis for FGF receptor dimerization and activation. *Cell* **98,** 641–650 (1999).
44. Emsley, P. & Cowtan, K. Coot: model-building tools for molecular graphics. *Acta Crystallogr. D* **60,** 2126–2132 (2004).
45. Suzuki, M. *et al*. βKlotho is required for fibroblast growth factor (FGF) 21 signaling through FGF receptor (FGFR) 1c and FGFR3c. *Mol. Endocrinol.* **22,** 1006–1014 (2008).
46. Ornitz, D. M. *et al.* FGF binding and FGF receptor activation by synthetic heparan-derived di- and trisaccharides. *Science* **268,** 432–436 (1995).
47. Liu, Y. *et al.* Regulation of receptor binding specificity of FGF9 by an autoinhibitory homodimerization. *Structure* **25,** 1325–1336 (2017).
48. Belov, A. A. & Mohammadi, M. Molecular mechanisms of fibroblast growth factor signaling in physiology and pathology. *Cold Spring Harb. Perspect. Biol*. **5,** a015958 (2013).
49. Beenken, A., Eliseenkova, A. V., Ibrahimi, O. A., Olsen, S. K. & Mohammadi, M. Plasticity in interactions of fibroblast growth factor 1 (FGF1) N terminus with FGF receptors underlies promiscuity of FGF1. *J. Biol. Chem.* **287,** 3067–3078 (2012).
50. Olsen, S. K. *et al.* Structural basis by which alternative splicing modulates the organizer activity of FGF8 in the brain. *Genes Dev* **20,** 185–198 (2006).
51. Robinson, C. J., Harmer, N. J., Goodger, S. J., Blundell, T. L. & Gallagher, J. T. Cooperative dimerization of fibroblast growth factor 1 (FGF1) upon a single heparin saccharide may drive the formation of 2:2:1 FGF1.FGFR2c.heparin ternary complexes. *J. Biol. Chem.* **280,** 42274–42282 (2005).
52. Goodger, S. J. *et al.* Evidence that heparin saccharides promote FGF2 mitogenesis through two distinct mechanisms. *J. Biol. Chem.* **283,** 13001–13008 (2008).
53. Dunshee, D. R. *et al.* Fibroblast activation protein cleaves and inactivates fibroblast growth factor 21. *J. Biol. Chem.* **291,** 5986–5996 (2016).

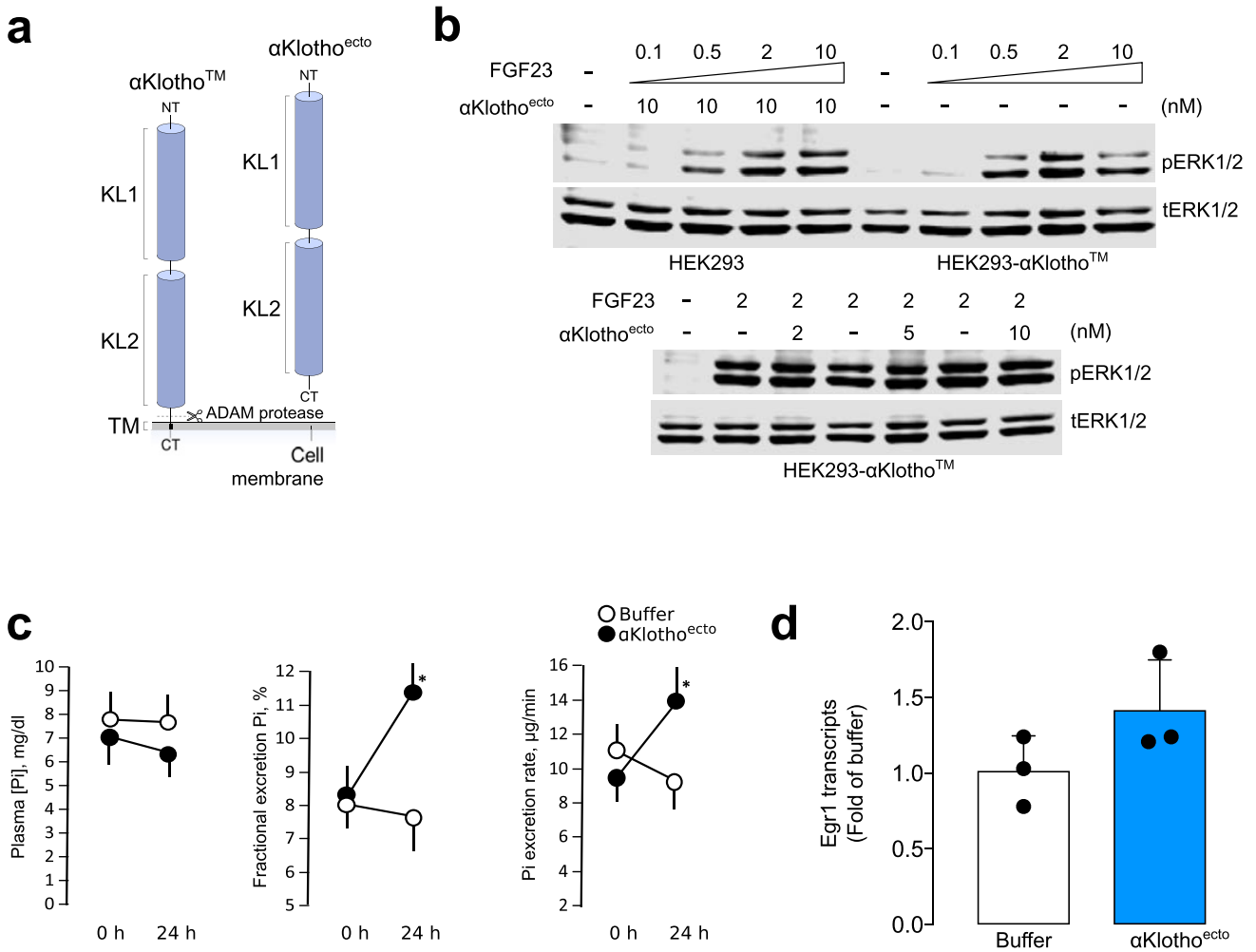

Extended Data Figure 1 | α-Klotho^{ecto} functions as a co-receptor for FGF23. a, Domain organization of membrane-bound α-klotho (α-klotho^{TM}) and its soluble isoform α-klotho^{ecto} generated by an ectodomain shedding in the kidney[16]. KL1 and KL2 are tandem domains with homology to family 1 glycosidases[8]. **b**, Representative immunoblots of phosphorylated ERK (top) and total ERK (bottom; sample loading control) in total HEK293 cell lysates ($n = 3$ independent experiments). Top, lysates from untransfected HEK293 cells that were pre-treated with a fixed α-klotho^{ecto} concentration (10 nM) and then stimulated with increasing FGF23 concentrations, and lysates from HEK293-α-klotho^{TM} cells treated with increasing concentrations of FGF23 alone. Bottom, lysates from HEK293-α-klotho^{TM} cells that were pre-treated with increasing α-klotho^{ecto} concentrations and then stimulated with a fixed FGF23 concentration. **c**, Plasma phosphate, fractional excretion of phosphate, and phosphate excretion rate in wild-type mice before and after a single injection of α-klotho^{ecto} (0.1 mg kg^{-1} body weight) or isotonic saline alone (buffer). Circles denote mean values; error bars denote s.d. $n = 10$ mice per group. *$P < 0.05$, paired Student's t test. **d**, Relative *Egr1* mRNA levels in the kidney of wild-type mice after a single injection with α-klotho^{ecto} (0.1 mg kg^{-1} body weight) or isotonic saline alone (buffer). Data are mean and s.d. $n = 3$ mice per group. The same batch of α-klotho^{ecto} protein was used in the experiments shown in **b**–**d**.

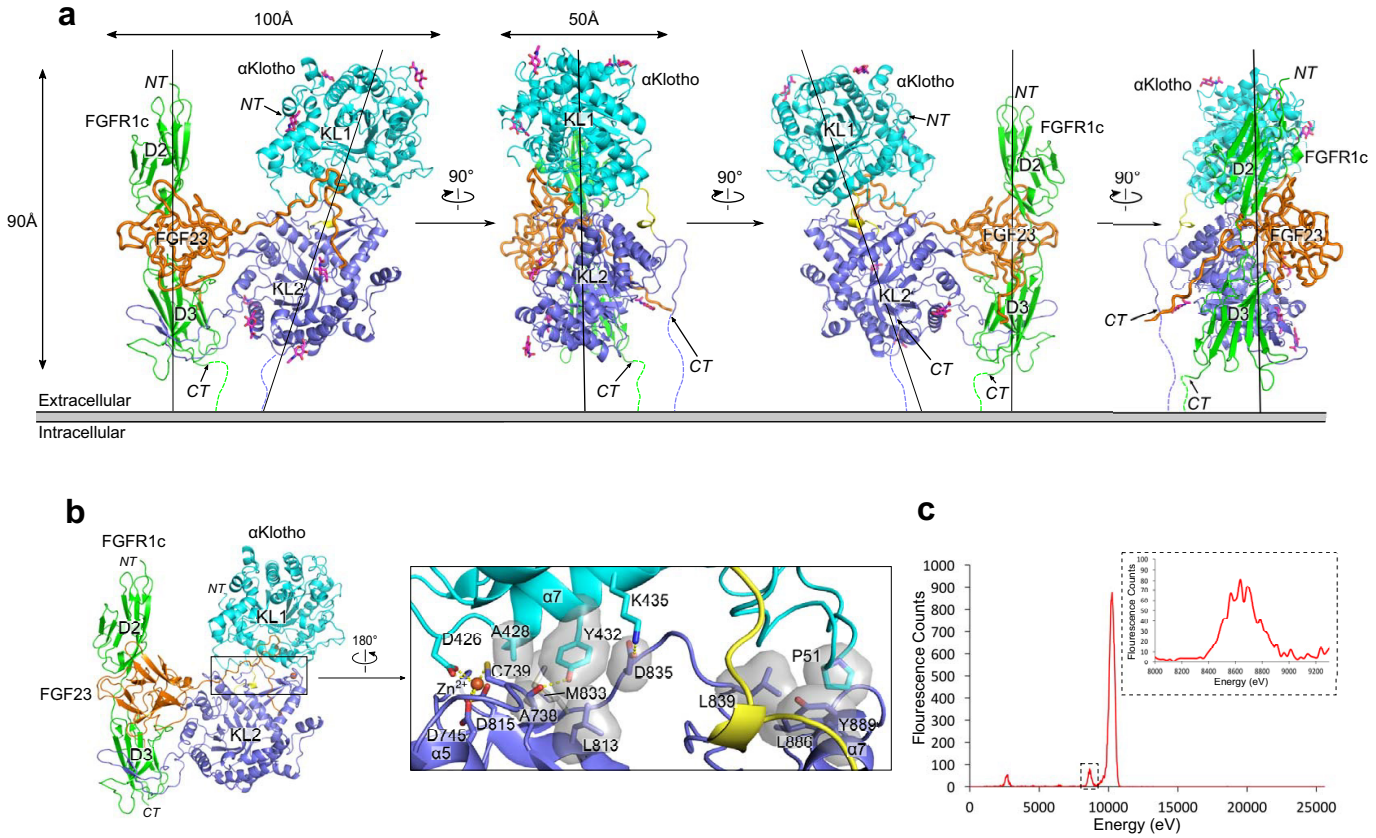

Extended Data Figure 2 | Topology of ternary complex is consistent with its orientation on the cell surface. a, Cartoon representation of 1:1:1 FGF23–FGFR1c^{ecto}–α-klotho^{ecto} complex in four different orientations related by 90° rotation. α-Klotho domains are coloured cyan (KL1) and blue (KL2); the KL1–KL2 linker is in yellow. FGFR1c and FGF23 are in green and orange, respectively. The ternary complex resembles an oblique rectangular prism with an average dimension of 100 Å × 90 Å × 50 Å. The long axes of α-klotho^{ecto} and FGF23–FGFR1c complex in the ternary complex are each about 90 Å long, and parallel to one another such that the C termini of FGFR1c^{ecto} and α-klotho^{ecto} end up on the same side of the ternary complex, ready to insert into the cell membrane (grey bar). First, the *N*-acetyl glucosamine moiety (purple sticks) at six of the seven consensus *N*-linked α-klotho glycosylation sites could be built owing to sufficient electron density. Asn694 is the only glycosylation site that falls in the vicinity of a binding interface, namely α-klotho^{ecto}–FGF23. **b**, Close-up view of the KL1–KL2 interdomain interface. Zinc (orange sphere)-mediated contacts facilitate overall α-klotho^{ecto} conformation. Dashed yellow lines denote hydrogen bonds; grey surfaces denote hydrophobic contacts. **c**, Emission energy spectrum obtained from excitation/emission scan of the FGF23–FGFR1c^{ecto}–α-klotho^{ecto} crystal. Inset shows an expanded view of zinc fluorescence at 8,637 eV of emission energy.

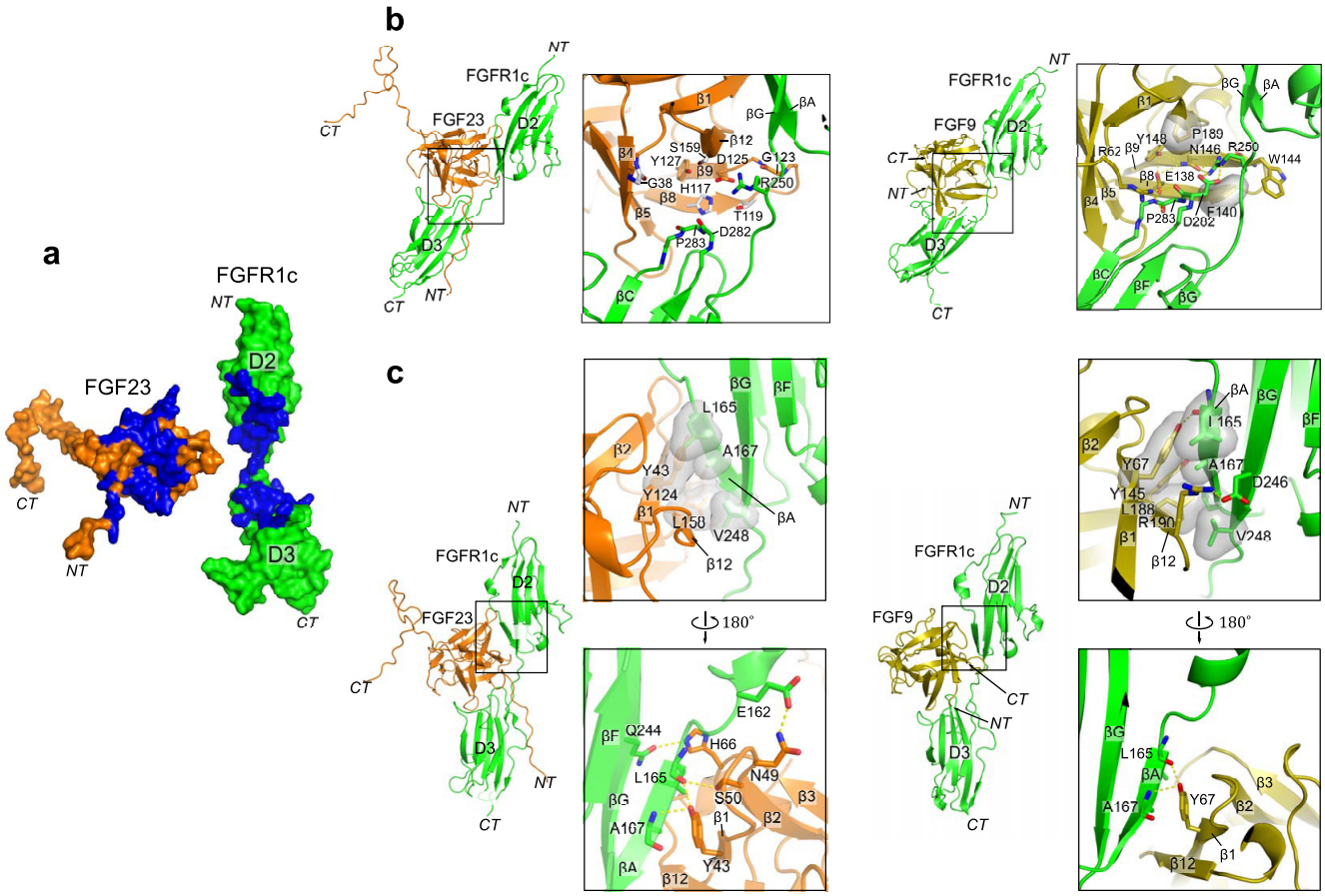

Extended Data Figure 3 | Structural basis for the weak FGFR-binding affinity of FGF23. a, Open-book view of FGF23–FGFR1c^{ecto} complex interface. FGF23 (orange) and FGFR1c^{ecto} (green) are pulled apart and rotated by 90° around the vertical axis to expose the binding interface (blue). **b**, Ligand–receptor D3 and ligand–receptor D2–D3 linker interfaces of endocrine FGF23–FGFR1c and paracrine FGF9–FGFR1c[47] structures. Grey transparent surfaces denote hydrophobic interactions; dashed yellow lines denote hydrogen bonds. Because FGF9 Arg62 is replaced with glycine in FGF23 (Gly38) and FGF9 Glu138 is replaced with histidine in FGF23 (His117), neither the side chain of Asp125 in FGF23 (Asn146 in FGF9), nor the side chain of invariant Arg250 in the FGFR1c D2–D3 linker can be tethered through intramolecular hydrogen bonds. Thus, these side chains possess greater freedom of motion in the FGF23–FGFR1c complex, and as a result, hydrogen bonding between FGF23 and FGFR1c D2–D3 linker entails greater entropic cost, which generates less binding affinity. Substitution of Phe140 and Pro189 in FGF9 with hydrophilic Thr119 and Ser159 in FGF23 further diminishes the ability of FGF23 to gain binding affinity from hydrogen bonding with FGFR1c D2–D3 linker. A lack of contacts between FGF23 N terminus and FGFR1c D3 cleft, which forms between alternatively spliced βC′-βE and βB′-βC loops[48], probably further exacerbates the weak FGFR-binding affinity of FGF23. **c**, Ligand–receptor D2 interface in endocrine FGF23–FGFR1c and paracrine FGF9–FGFR1c[47] structures. Grey transparent surfaces denote hydrophobic interactions; dashed yellow lines denote hydrogen bonds. Many contacts at this interface are conserved between paracrine FGF molecules and FGF23, and hence FGF23 gains much of its FGFR-binding affinity through these contacts. Three hydrogen bonds involving Asn49, Ser50 and His66 of FGF23 are unique to the FGF23–FGFR1c complex.

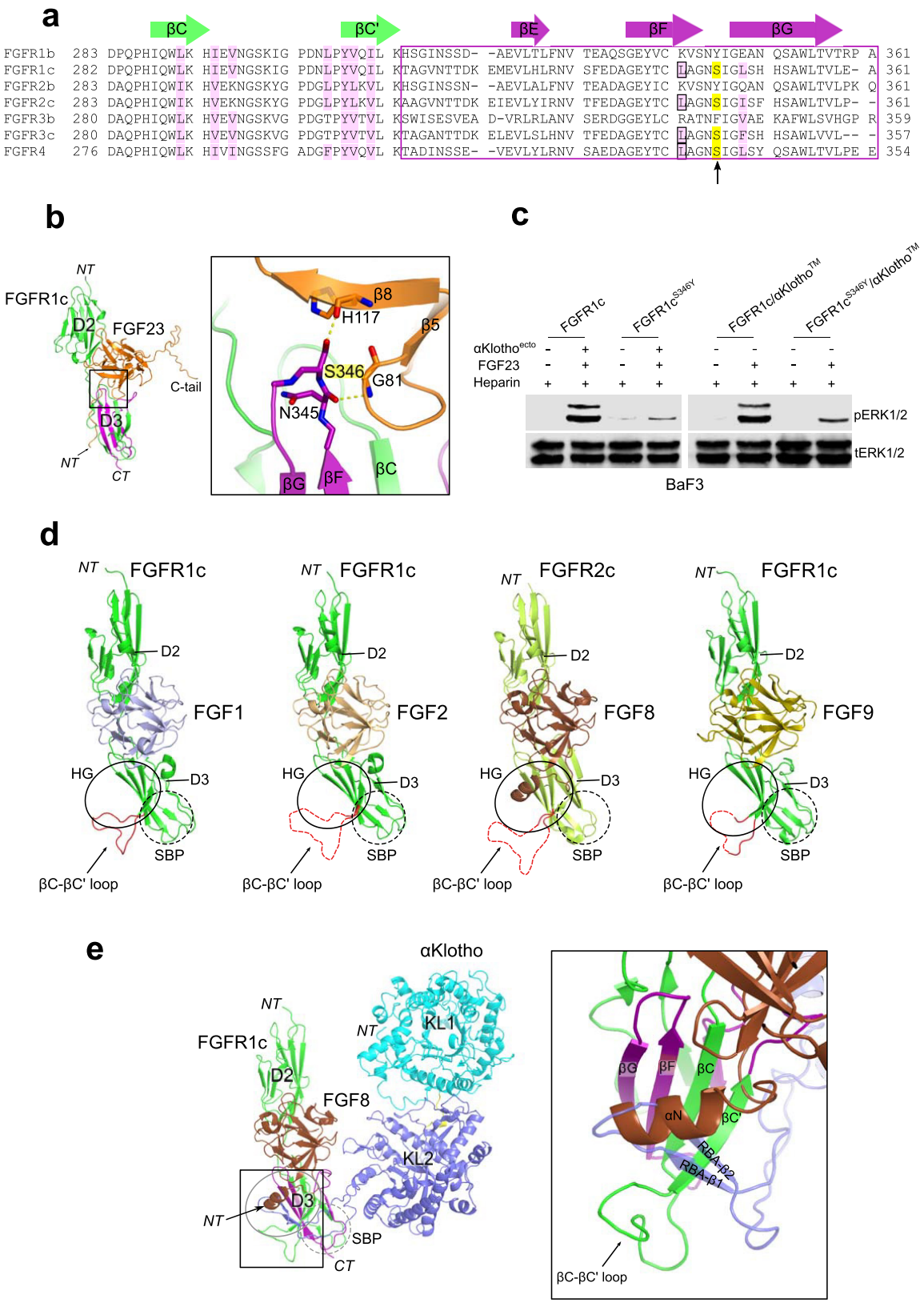

Extended Data Figure 4 | See next page for caption.

Extended Data Figure 4 | Structural basis for FGFR isoform specificity of α-klotho and FGF23. a, Structure-based sequence alignment of a segment of FGFR D3. The alternatively spliced regions of all seven FGFRs are boxed with a purple rectangle. β-strand locations above the alignment are coloured green (constant region) and purple (alternatively spliced region). A leucine (boxed) of hydrophobic groove residues (light purple) in the alternatively spliced region is conserved only among 'c' isoforms of FGFR1–FGFR3 and FGFR4, which explains α-klotho binding selectivity for these receptors. **b**, Interface between FGF23 and the βF–βG loop of FGFR1c D3 in the FGF23–FGFR1c structure of the ternary complex. Backbone atoms of His117 and Gly81 in FGF23 make specific hydrogen bonds with the Ser346 side-chain and Asn345 backbone atoms of the βF–βG loop. The serine residue corresponding to Ser346 in FGFR1c (yellow) is conserved only among 'c' isoforms of FGFR1–FGFR3 and FGFR4 (see **a**). **c**, Representative immunoblots of phosphorylated ERK (top) and total ERK (bottom; sample loading control) in total BaF3 cell lysates ($n = 3$ independent experiments). **d**, Cartoon representations of four paracrine FGF–FGFR complex structures[4,47,49,50]. Solid black oval denotes the hydrophobic D3 groove. Dashed black circle denotes the second binding pocket (SBP) for α-klotho in D3. Although the hydrophobic groove is engaged by FGF8 (see also **e**), the SBP is not used in any of the current paracrine FGF–FGFR structures. In most paracrine FGF–FGFR structures, the βC-βC′ loop is disordered (dashed red lines) because it does not participate in FGF binding. Evidently, SBP and βC-βC′ loop in D3 have evolved to mediate α-klotho binding to FGFR. **e**, α-Klotho and FGF8b both bind to the hydrophobic groove in FGFR1c D3. FGF8b (brown) from the FGF8b–FGFR2c structure[50] was superimposed onto FGF23 in the FGF23–FGFR1c^{ecto}–α-klotho^{ecto} complex. The αN helix of FGF8b occupies the same binding pocket in FGFR1c D3 as the distal tip of the α-klotho RBA.

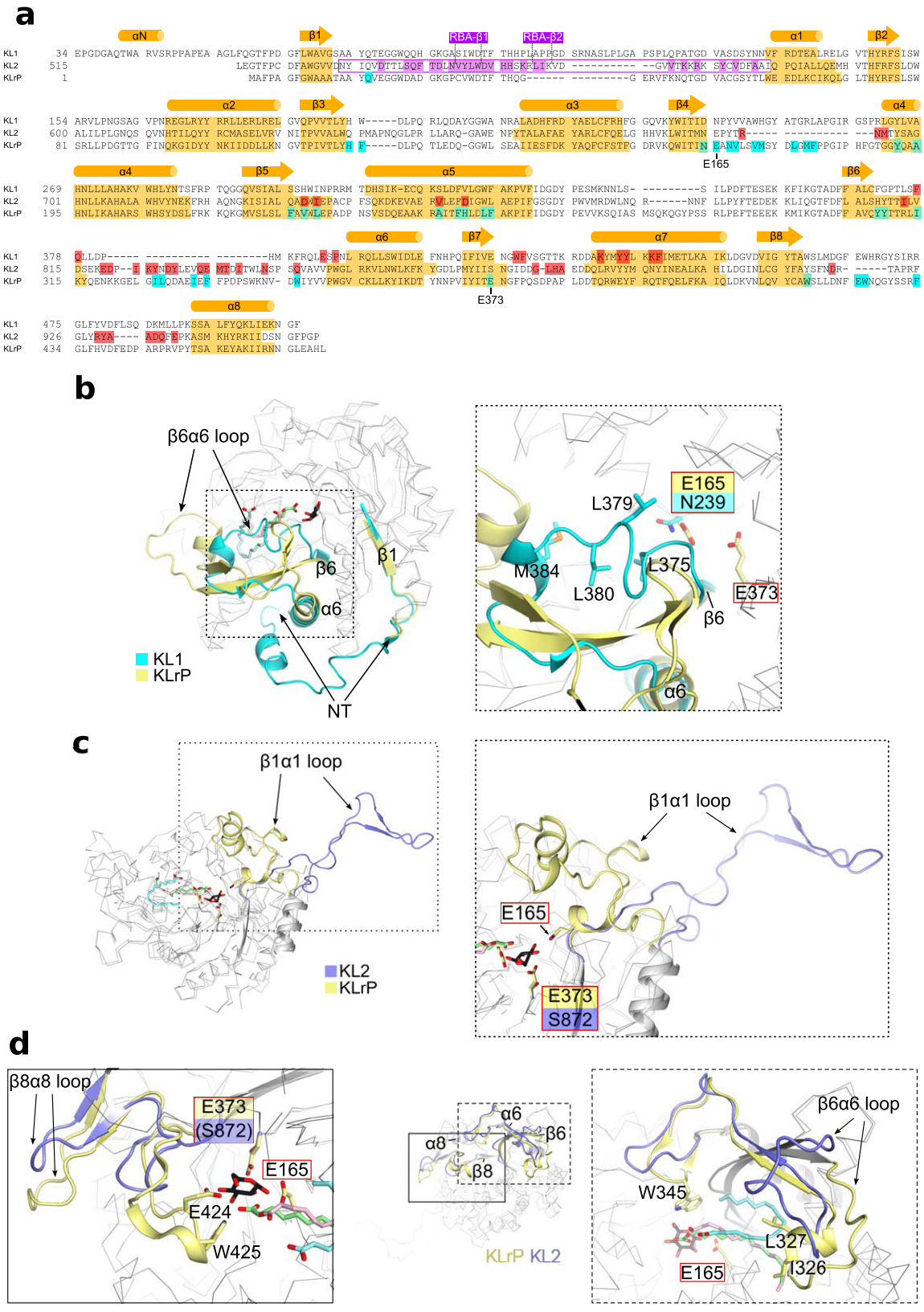

Extended Data Figure 5 | See next page for caption.

Extended Data Figure 5 | α-Klotho is the first non-enzymatic scaffold among TIM barrel proteins. a, Structure-based sequence alignment of TIM barrels of α-klotho KL1 and KL2 domains and KLrP. Most glycoside hydrolases (GH), a functionally diverse group of enzymes that cleave glycosidic bonds of complex carbohydrates on glycoproteins[8], adopt a TIM barrel fold. Locations and lengths of TIM barrel β-strands and α-helices are indicated above the alignment. Among GH family 1 members of the klotho subfamily, only KLrP has a verified glycosylceramidase activity[26], and Glu165 and Glu373 are its catalytically essential glutamic acids. KLrP residues coloured cyan participate in substrate recognition/hydrolysis. α-Klotho residues coloured red bind FGF23, and α-klotho residues of the KL2 β1α1 loop (purple box) coloured purple interact with the FGFR1c D3 domain. **b**, Superimposition of KL1 C_α trace (grey/cyan) onto that of KLrP (grey/yellow). Superimposition root mean square deviation (r.m.s.d.) value is 1.08 Å. Structurally most divergent regions between KL1 and KLrP are in cartoon representation. Glucose moiety and aliphatic chains of glucosylceramide (KLrP substrate) are in sticks with carbon in black (glucose) or green/cyan/pink (aliphatic chains). Catalytically essential Glu165 in KLrP is replaced by an asparagine in KL1. Hydrophobic residues from KL1 β6α6 loop occupy the pocket that accommodates the aliphatic chains of glucosylceramide in KLrP. The KL1 N terminus supports KL1–KL2 cleft formation (Extended Data Fig. 2b) and KL1 β6α6 loop conformation contributes to a key portion of the binding pocket in this cleft for the FGF23 C-terminal tail (Fig. 3c). **c**, **d**, Superimposition of KL2 C_α trace (grey/blue) onto that of KLrP (grey/yellow). Superimposition r.m.s.d. value is 1.37 Å. Structurally divergent β1α1 (**c**), β6α6 and β8α8 (**d**) loops of KL2 and KLrP are rendered in cartoon. β1α1 loop in KL2 is disengaged from the central TIM barrel and stretches away from it by as much as 35 Å. Catalytically essential Glu373 in KLrP is replaced by a serine in KL2. KLrP residues from β6α6 and β8α8 loops bind glucosylceramide (KLrP substrate); for example, Trp345 in the β6α6 loop and Glu424 and Trp425 in the β8α8 loop. Sequence divergence (**a**) and altered loop conformations are incompatible with glucosylceramide coordination by KL2. β1α1, β6α6 and β8α8 loops lie at the rim of the catalytic mouth in the TIM barrel (see Fig. 2b). Divergent conformations of these three loops in KL2 result in notable widening of the central barrel cavity in KL2, which merges with the KL1–KL2 cleft to form an expansive basin that accommodates the distal portion of the FGF23 C-terminal tail.

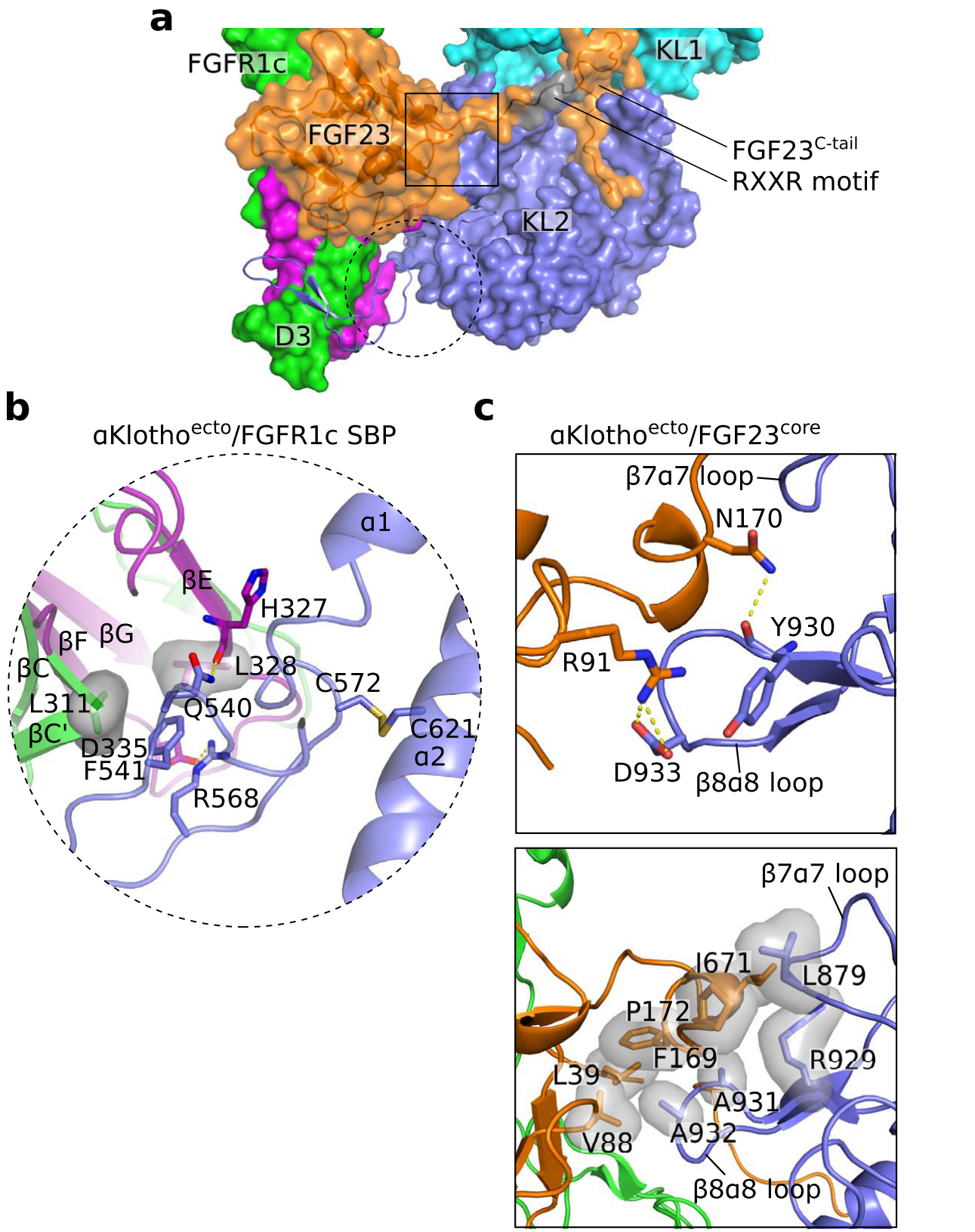

Extended Data Figure 6 | α-Klotho interaction with rigid core of FGF23 and a second binding pocket next to the hydrophobic groove in FGFR1c D3. a, A partial view of the ternary complex. α-Klotho^{ecto} (cyan/blue solid surface, RBA of KL2 in blue cartoon), FGF23 (orange transparent surface and cartoon), FGFR1c (constant region: solid green surface; alternatively spliced region: solid purple surface). Dashed black circle denotes the perimeter of the interface between proximal end of α-klotho RBA and a second binding pocket (SBP) in FGFR1c D3 next to the hydrophobic groove. Solid black box denotes the perimeter of α-klotho–FGF23^{core} interface. **b**, Close-up view of the interface between proximal end of RBA and SBP in D3. The disulfide bridge between Cys572 (N-terminal end of RBA) and Cys621 (α2 helix) at the base of the RBA probably imparts some degree of conformational rigidity to the proximal RBA portion, whereas the conformation of the distal RBA tip is dictated by contacts with FGFR1c D3. **c**, Close-up view of the α-klotho–FGF23^{core} interface detailing hydrogen bonding (top) and hydrophobic contacts (bottom). Grey transparent surfaces denote hydrophobic interactions; dashed yellow lines denote hydrogen bonding contacts.

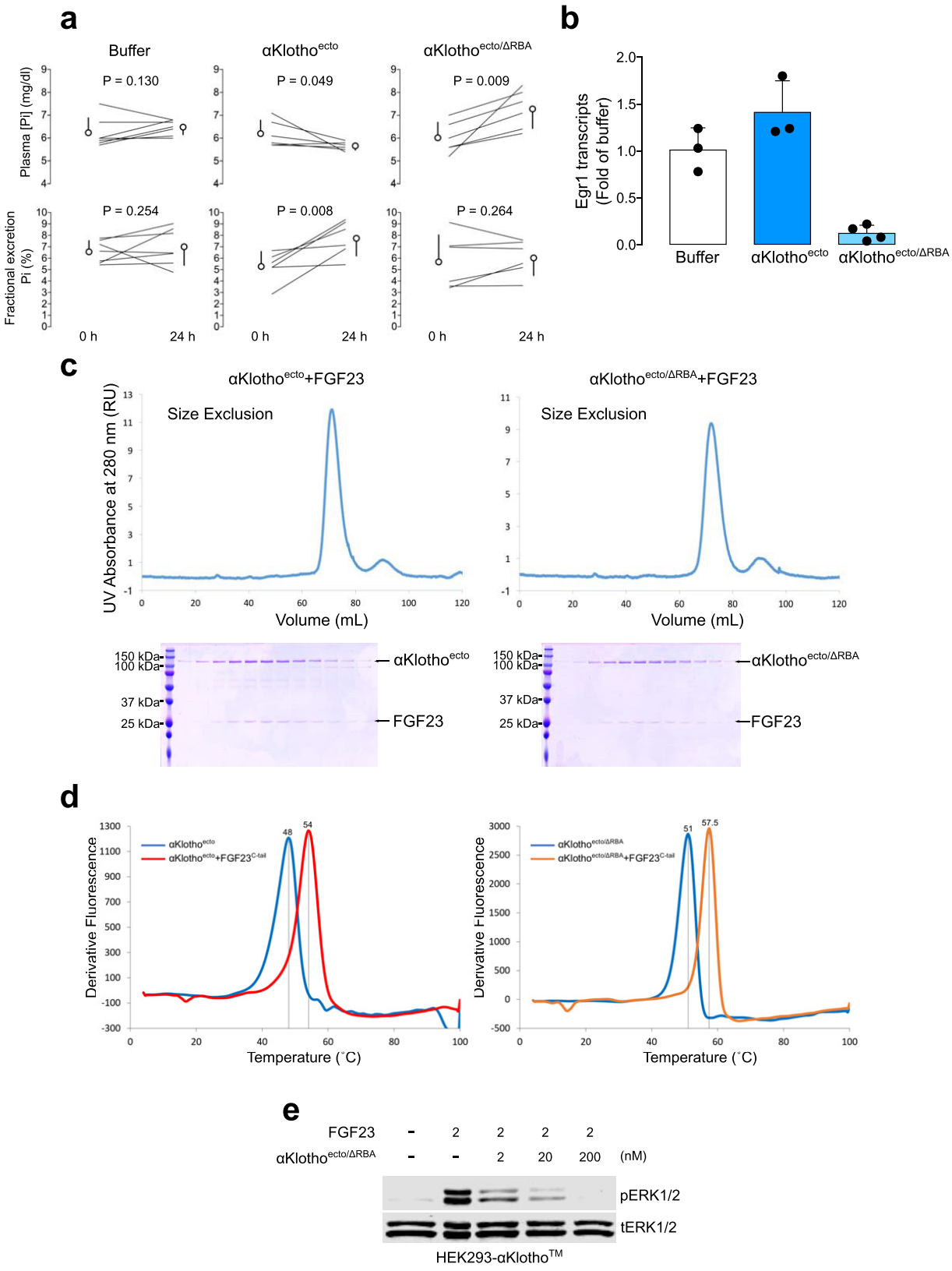

Extended Data Figure 7 | See next page for caption.

Extended Data Figure 7 | Deletion of RBA of α-klotho^{ecto} generates an FGF23 ligand trap. a, Plasma phosphate and fractional excretion of phosphate in wild-type mice before and after a single injection of α-klotho^{ecto} (0.1 mg kg^{-1} body weight), mutant α-klotho$^{ecto/\Delta RBA}$ (0.1 mg kg^{-1} body weight), or isotonic saline alone (buffer). Circles denote mean values; error bars denote s.d. $n = 6$ mice per group. Significance values were determined by a paired Student's *t* test. **b**, Relative *Egr1* mRNA levels in the kidney of wild-type mice injected once with α-klotho^{ecto} (0.1 mg kg^{-1} body weight; $n = 3$), mutant α-klotho$^{ecto/\Delta RBA}$ (0.1 mg kg^{-1} body weight; $n = 4$), or isotonic saline alone (buffer; $n = 3$). Data are mean and s.d. **c**, Representative elution profiles of FGF23–α-klotho^{ecto} and FGF23–α-klotho$^{ecto/\Delta RBA}$ mixtures from a size-exclusion column and representative Coomassie blue-stained SDS-polyacrylamide gels of eluted protein peak fractions. **d**, Thermal shift assay of α-klotho^{ecto} and the α-klotho$^{ecto/\Delta RBA}$ mutant in the presence and absence of FGF23 C-terminal tail peptide (FGF23$^{C\text{-}tail}$) ($n = 3$ independent experiments). Increased melting temperatures in the presence of the FGF23$^{C\text{-}tail}$ indicate interaction of both α-klotho^{ecto} proteins with the peptide. Higher melting temperature of α-klotho$^{ecto/\Delta RBA}$ mutant relative to wild-type α-klotho^{ecto} indicates greater stability of the mutant protein. **e**, Representative immunoblots of phosphorylated ERK (top) and total ERK (bottom; sample loading control) in total lysates from HEK293-α-klotho^{TM} cells co-stimulated with a fixed FGF23 concentration and increasing α-klotho$^{ecto/\Delta RBA}$ concentrations ($n = 3$ independent experiments). The α-klotho$^{ecto/\Delta RBA}$ mutant inhibits FGF23-induced ERK phosphorylation owing to sequestering FGF23 into inactive FGF23–α-klotho$^{ecto/\Delta RBA}$ binary complexes. This also explains why α-klotho$^{ecto/\Delta RBA}$ injection into mice causes an increase in plasma phosphate (**a**) concomitant with renal *Egr1* gene repression (**b**).

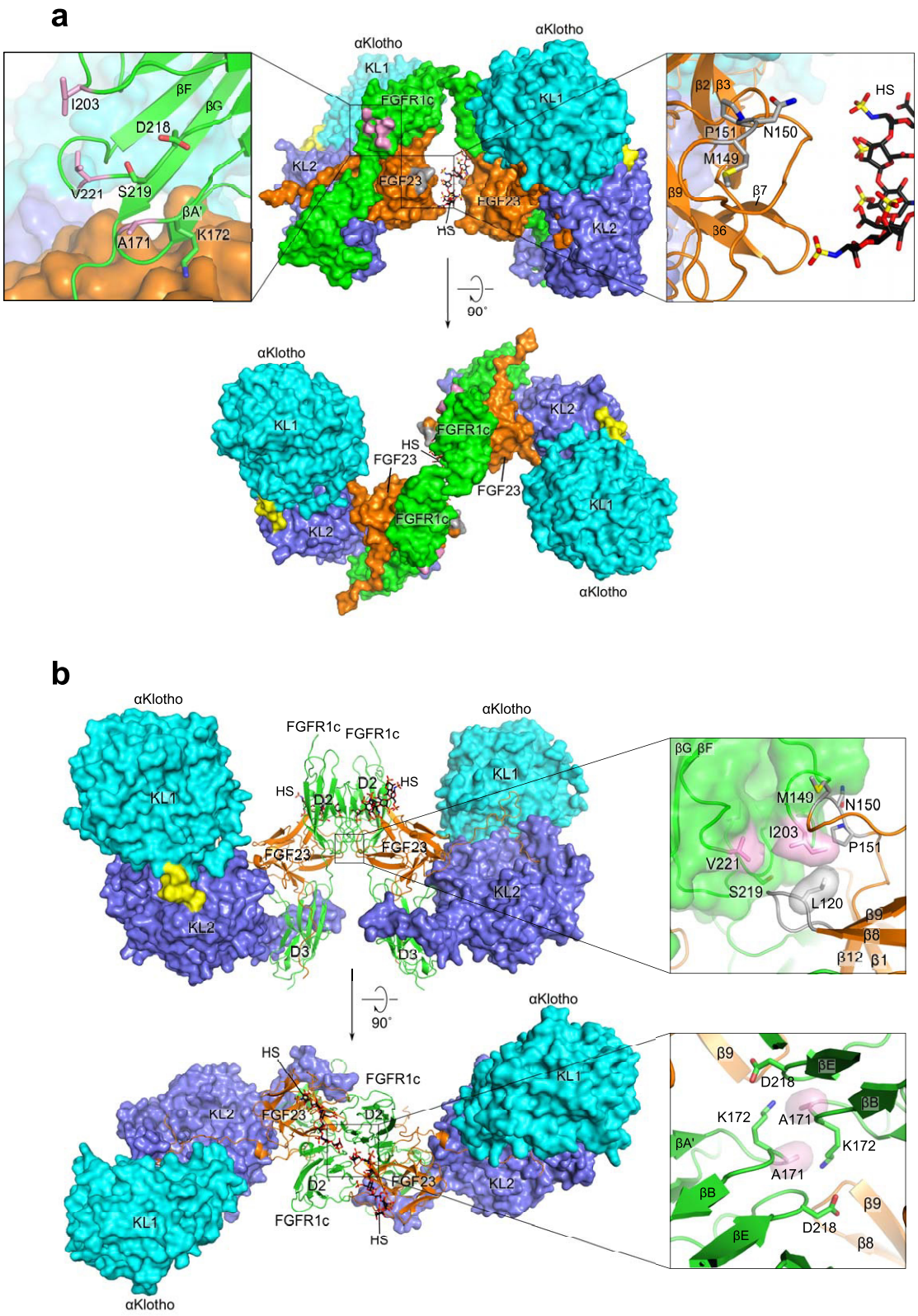

Extended Data Figure 8 | See next page for caption.

Extended Data Figure 8 | FGF23–FGFR1c^{ecto}–α-klotho^{ecto}–HS quaternary dimer models. a, A 2:2:2:1 FGF23–FGFR1c^{ecto}–α-klotho^{ecto}–HS quaternary dimer in two orientations related by a 90° rotation around the horizontal axis. The dimer was constructed by superimposing FGF23 from two copies of 1:1:1 FGF23–FGFR1c^{ecto}–α-klotho^{ecto} complex onto the two FGF1 molecules in the 2:2:1 FGF1–FGFR2c–HS dimer[30,31,51,52]. The dimer is held together solely by HS, which bridges two FGF23 molecules in *trans*. Boxed pink surface denotes the location of Ala171, Ile203 and Val221 of FGFR1c, the mutation of which impairs the ability of HS to induce 2:2:2:2 quaternary dimer formation (Fig. 5f). Boxed grey region denotes the location of Met149, Asn150 and Pro151 of FGF23, the mutation of which diminishes HS-induced quaternary dimerization (Fig. 5e, f). None of these residues has any role in 2:2:2:1 quaternary dimer formation, and hence, contrary to experimental evidence (Fig. 5), mutation of these residues should not affect HS-induced FGF23–FGFR1c^{ecto}–α-klotho^{ecto} dimerization. **b**, A 2:2:2:2 FGF23–FGFR1c^{ecto}–α-klotho^{ecto}–HS quaternary dimer in two orientations related by a 90° rotation around the horizontal axis. See also Fig. 5g. The dimer was constructed by superimposing FGF23 from two copies of 1:1:1 FGF23–FGFR1c^{ecto}–α-klotho^{ecto} complex onto the two FGF2 molecules in the 2:2:2 FGF2–FGFR1c–HS dimer[4]. Insets show close-up views of the secondary FGF–FGFR (top) and direct FGFR–FGFR (bottom) interfaces. Grey/pink transparent surfaces denote hydrophobic interactions. Mutation of Ala171, Ile203 and Val221 (pink) impairs the ability of HS to dimerize the FGF23–FGFR1c^{ecto}–α-klotho^{ecto} ternary complex (Fig. 5f).

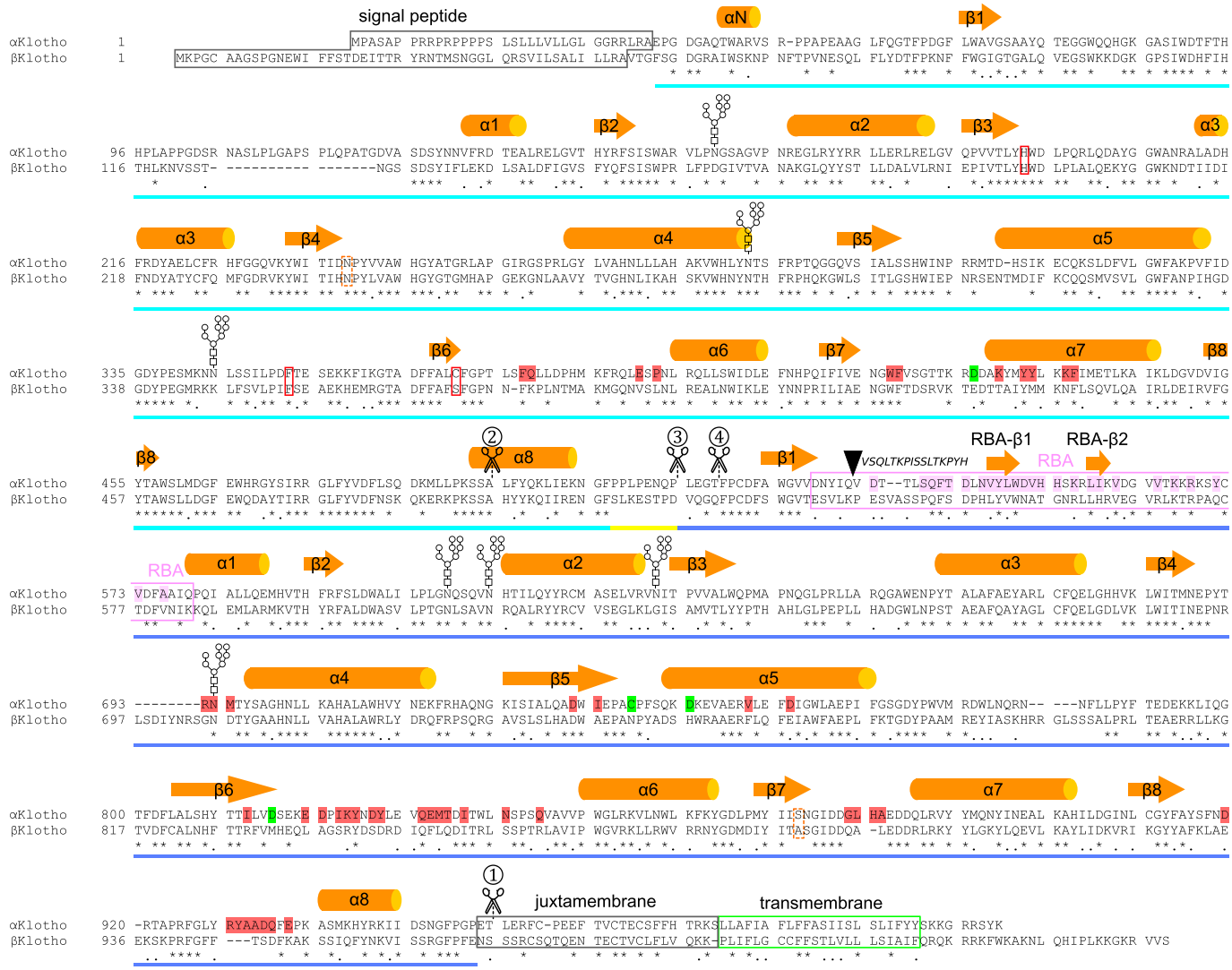

Extended Data Figure 9 | The FGF19 and FGF21 co-receptor β-klotho is a non-enzymatic scaffold protein analogous to α-klotho. Structure-based sequence alignment of α-klotho and β-klotho. The locations of the eight alternating β-strands and α-helices of the TIM fold are indicated above the alignment. Cyan, blue and yellow bars below the alignment mark the domain boundaries of KL1, KL2 and the KL1–KL2 linker. Asterisks denote sequence identity and dots denote sequence similarity. Scissor symbols mark the four proposed sites of α-klotho cleavage by ADAM proteases/secretases. Cleavage 1, which coincides with the end of the rigid core of KL2, results in shedding of the entire α-klotho ectodomain from the cell membrane. Although this cleavage product is a functional co-receptor, the α-klotho fragments generated by cleavages 2, 3 and 4 would be devoid of co-receptor activity. Black triangle denotes the site where alternative splicing replaces the C-terminal KL2 sequence with a 15-residue-long unrelated sequence. Glycan chain symbols denote seven predicted *N*-linked glycosylation sites. Zn^{2+}-chelating residues of α-klotho are green, FGFR1c-binding residues are light purple, and FGF23-binding residues are red. Light purple box denotes β1α1 loop sequence in KL2 termed RBA. β-Klotho RBA is about as long as α-klotho RBA, and key FGFR-binding residues are conserved between these two RBAs, which is consistent with the similar FGFR-binding specificity of α-klotho and β-klotho[9,11,12]. But α-klotho residues in the binding pockets for the FGF23 C-terminal tail are not conserved in β-klotho, conforming to major sequence differences between the C-terminal tails of FGF23, FGF19 and FGF21 (Extended Data Fig. 10a).

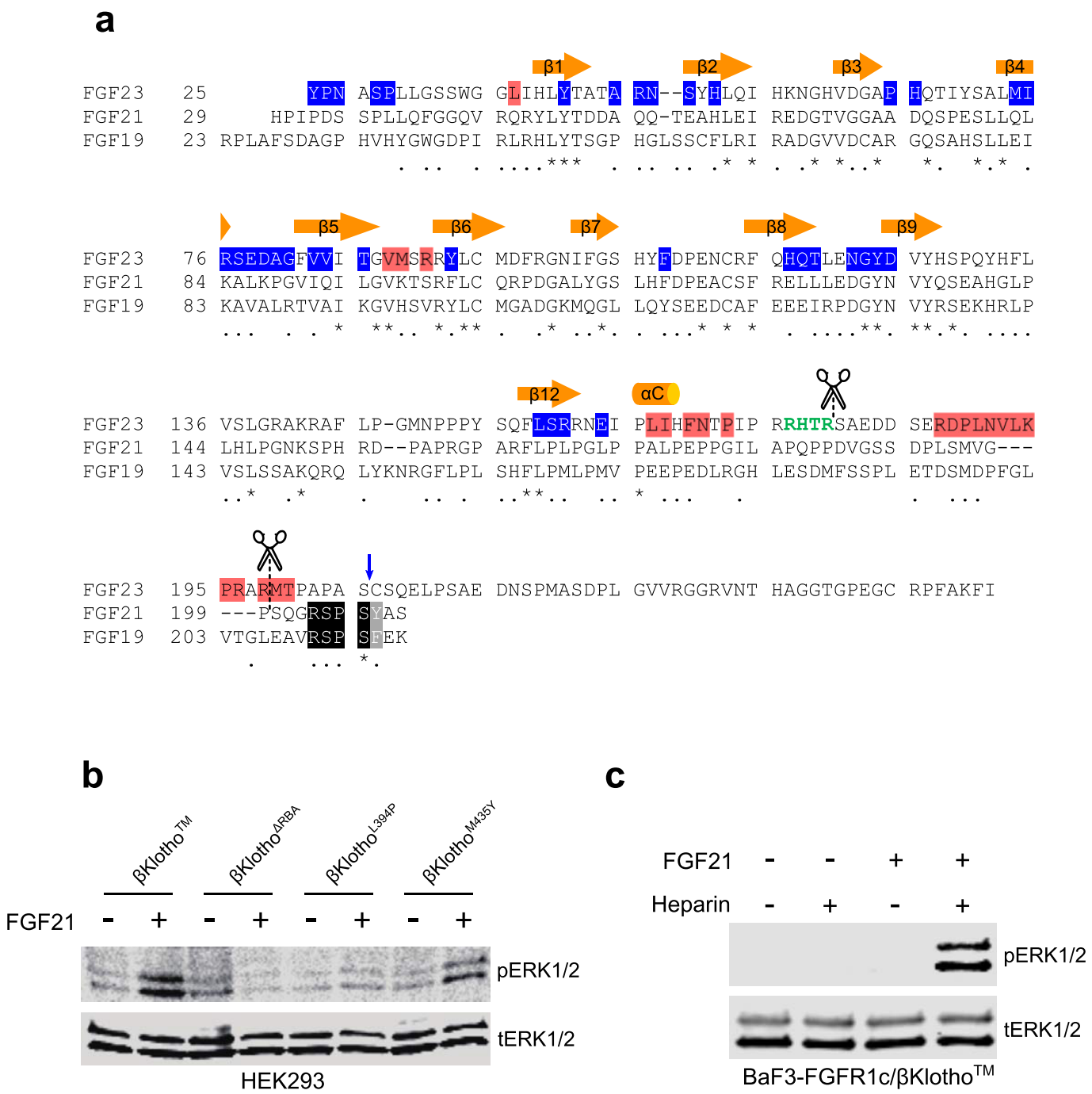

Extended Data Figure 10 | β-Klotho-dependent FGFR activation by FGF19 and FGF21 is mechanistically similar to α-klotho-dependent FGFR activation by FGF23. a, Structure-based sequence alignment of endocrine FGF proteins. β-strands and the αC helix comprising the atypical β-trefoil core of FGF23 are indicated above the alignment. Asterisks and dots below the alignment denote sequence identity and similarity, respectively. Scissor symbols mark inactivating proteolytic cleavage sites in FGF23 and FGF21[53]. RXXR cleavage motif in FGF23 is in green bold letters. FGFR1c-binding residues of FGF23 are coloured blue, α-klotho-binding residues are coloured red. Vertical blue arrow marks the C-terminal boundary of the FGF23 variant used to solve the FGF23–FGFR1c^{ecto}–α-klotho^{ecto} complex structure. Five residues at the distal C-terminal region of FGF19 or FGF21 (black and grey) mediate binding of FGF19 or FGF21 to β-klotho. These residues completely diverge from the α-klotho-binding residues in the FGF23 C-terminal tail. α-Klotho-binding residues in the FGF23 core also are not conserved in FGF19 and FGF21. **b**, Representative immunoblots of phosphorylated ERK (top) and total ERK (bottom; sample loading control) in total lysates from HEK293 cells expressing wild-type or mutant β-klotho^{TM} ($n = 3$ independent experiments). Similar to α-klotho$^{\Delta RBA}$, β-klotho$^{\Delta RBA}$ failed to support FGF21-induced FGFR activation, and β-klotho (L394P) and β-klotho (M435Y) mutants also had greatly diminished ability to promote FGF21 signalling. Thus, β-klotho tethers FGFR1c and FGF21 to itself in a manner similar to that identified for α-klotho to enable FGF21 signalling. **c**, Representative immunoblots of phosphorylated ERK (top) and total ERK (bottom; sample loading control) in total lysates from BaF3 cells expressing FGFR1c and β-klotho^{TM} ($n = 3$ independent experiments). Like α-klotho, β-klotho also requires heparin to support FGF21-mediated FGFR1c activation.

Extended Data Table 1 | X-ray data collection and structure refinement statistics

Protein	FGF23-FGFR1c^{ecto}-αKlotho^{ecto}
Data Collection	
X-ray wavelength (Å)	0.97918
Space group	C2
Unit Cell Dimensions	
a, b, c (Å)	283.31, 72.60, 95.33
α, β, γ (°)	90.00, 91.98, 90.00
Resolution (Å)	50-3.00 (3.18-3.0)
No. measured reflections	294862
No. unique reflections	39077
Data redundancy	7.5 (7.6)
Data completeness (%)	99.7 (98.8)
R_{meas} (%)	20.7 (138.0)
Signal (<I/σI>)	11.1 (1.7)
Refinement	
Resolution (Å)	48.81-3.00 (3.08-3.00)
No. unique reflections	38950 (2688)
No. reflections (R_{free})	1947 (133)
R_{work}/R_{free}	23.00 (44.46)/27.82 (51.89)
No. TLS groups	3 (one per polypeptide chain)
Number of atoms	
Protein	10602
Sugar (NAG)	98
Ion (Zn^{2+})	1
Solvent	1
R.m.s. deviations	
Bond length (Å)	0.002
Bond angle (°)	0.483
Average B factors (Å^2)	
Protein	114
Sugar (NAG)	180
Ion (Zn^{2+})	116
Solvent	58
Ramachandran Plot	
Favored (%)	89.06
Allowed (%)	9.72
Outliers (%)	1.22
Rotamer outliers (%)	2.23
No. Cβ Deviations	0
All-Atom Clashscore	6.5
PDB ID	5W21

Values in parentheses are for the highest resolution shell.

nature research

Corresponding author(s): Moosa Mohammadi

☐ Initial submission ☐ Revised version ☒ Final submission

Life Sciences Reporting Summary

Nature Research wishes to improve the reproducibility of the work that we publish. This form is intended for publication with all accepted life science papers and provides structure for consistency and transparency in reporting. Every life science submission will use this form; some list items might not apply to an individual manuscript, but all fields must be completed for clarity.

For further information on the points included in this form, see Reporting Life Sciences Research. For further information on Nature Research policies, including our data availability policy, see Authors & Referees and the Editorial Policy Checklist.

Experimental design

1. Sample size

Describe how sample size was determined.

No statistical methods were used to determine sample size.

2. Data exclusions

Describe any data exclusions.

No data were excluded from the analyses.

3. Replication

Describe whether the experimental findings were reliably reproduced.

All attempts at replication were successful.

4. Randomization

Describe how samples/organisms/participants were allocated into experimental groups.

Wild-type mice were randomly divided into experimental groups with equal male and female number.

5. Blinding

Describe whether the investigators were blinded to group allocation during data collection and/or analysis.

For the data shown in Extended Data Fig. 7a, b, the investigators were blinded to allocation of mice to treatment groups during data collection and analysis.

Note: all studies involving animals and/or human research participants must disclose whether blinding and randomization were used.

6. Statistical parameters

For all figures and tables that use statistical methods, confirm that the following items are present in relevant figure legends (or in the Methods section if additional space is needed).

n/a	Confirmed
☐	☒ The exact sample size (*n*) for each experimental group/condition, given as a discrete number and unit of measurement (animals, litters, cultures, etc.)
☐	☒ A description of how samples were collected, noting whether measurements were taken from distinct samples or whether the same sample was measured repeatedly
☐	☒ A statement indicating how many times each experiment was replicated
☒	☐ The statistical test(s) used and whether they are one- or two-sided (note: only common tests should be described solely by name; more complex techniques should be described in the Methods section)
☒	☐ A description of any assumptions or corrections, such as an adjustment for multiple comparisons
☐	☒ The test results (e.g. *P* values) given as exact values whenever possible and with confidence intervals noted
☒	☐ A clear description of statistics including central tendency (e.g. median, mean) and variation (e.g. standard deviation, interquartile range)
☐	☒ Clearly defined error bars

See the web collection on statistics for biologists for further resources and guidance.

Software

Policy information about availability of computer code

7. Software

Describe the software used to analyze the data in this

NEBaseChanger v1.2.6 (New England Biolabs Inc., USA); Primer Design tool for In-

study.	Fusion HD Cloning Kit (Clontech Laboratories Inc., USA); ImageStudio Lite (LI-COR); Rock Maker (Formulatrix, USA); Rock Imager (Formulatrix, USA); HKL2000 (HKL Research, Inc., USA); Phenix suite v1.9_1692 (https://www.phenix-online.org/download/); COOT v0.8.2 (https://www2.mrc-lmb.cam.ac.uk/personal/pemsley/coot/binaries/release/); PyMOL (http://pymol.org/dsc/ip/); Empower PDA Software (Waters, USA); ASTRA (Wyatt Technology, USA); UNICORN (GE Healthcare, USA); GraphPad (GraphPad Software, Inc., USA); Microsoft Office Excel (Microsoft, USA);

For manuscripts utilizing custom algorithms or software that are central to the paper but not yet described in the published literature, software must be made available to editors and reviewers upon request. We strongly encourage code deposition in a community repository (e.g. GitHub). *Nature Methods* guidance for providing algorithms and software for publication provides further information on this topic.

Materials and reagents

Policy information about availability of materials

8. Materials availability

Indicate whether there are restrictions on availability of unique materials or if these materials are only available for distribution by a for-profit company.	No unique materials were used.

9. Antibodies

Describe the antibodies used and how they were validated for use in the system under study (i.e. assay and species).	Phosphorylated ERK1/2 (#4370, Rabbit mAb, Cell Signaling Technology, USA); Total (phosphorylated and unphosphorylated) ERK1/2 (#4695, Rabbit mAb, Cell Signaling Technology, USA); IRDye secondary antibody (#926-32211, goat anti-rabbit, LI-COR, USA); Klotho Antibody (E-21) (#SC-22220, Santa Cruz Biotechnology, USA); IRDye secondary antibody (#926-32214, Donkey anti-goat, LI-COR, USA). All of the antibodies were used for western experiments and were validated by the manufactures.

10. Eukaryotic cell lines

a. State the source of each eukaryotic cell line used.	N-acetylglucosaminytransferase I (GnTI) deficient HEK293S cells [#CRL-3022, American Type Culture Collection (ATCC), USA]; HEK293 cells (a gift from Dr. Alka Mansukhani, NYU Langone Medical Center); BaF3 cells (a gift from Dr. Sara Byron, TGen)
b. Describe the method of cell line authentication used.	All the cell lines are obtained from ATCC and hence are authenticated by the provider. The cell lines were also identified by morphology check under microscope in the lab.
c. Report whether the cell lines were tested for mycoplasma contamination.	Mycoplasma negative per DAPI staining.
d. If any of the cell lines used are listed in the database of commonly misidentified cell lines maintained by ICLAC, provide a scientific rationale for their use.	No commonly misidentified cell lines were used.

Animals and human research participants

Policy information about studies involving animals; when reporting animal research, follow the ARRIVE guidelines

11. Description of research animals

Provide details on animals and/or animal-derived materials used in the study.	129sv mouse strain, male and female, 6 weeks old, and 10 to 12 weeks old

Policy information about studies involving human research participants

12. Description of human research participants

Describe the covariate-relevant population characteristics of the human research participants.	This study did not involve human research participants.